Immunity

B cell-derived acetylcholine promotes liver regeneration by regulating Kupffer cell and hepatic CD8$^+$ T cell function

Graphical abstract

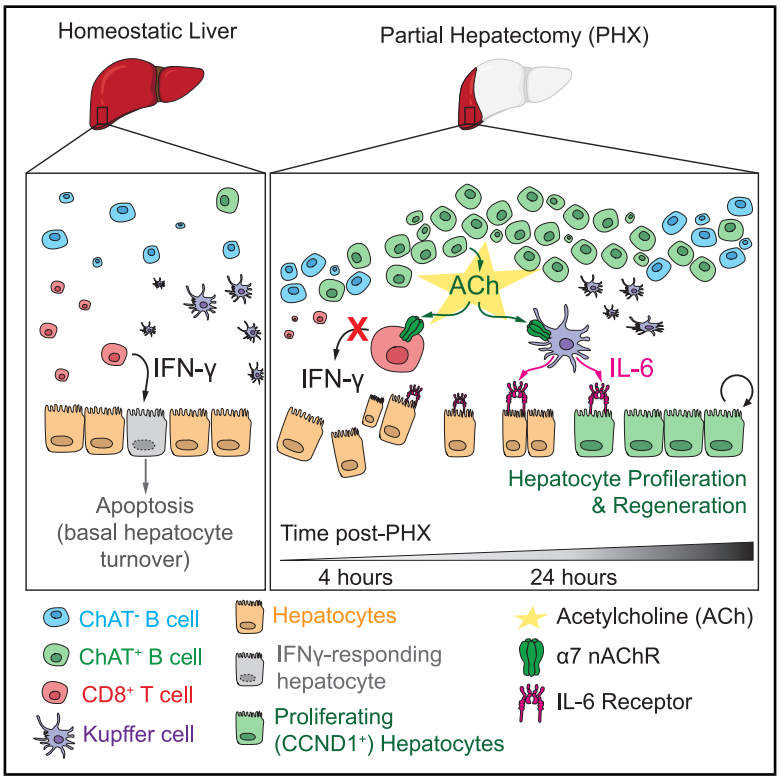

Highlights

- ChAT$^+$ B cells synthesize ACh early during LR, induced by partial hepatectomy
- Kupffer cells and hepatic CD8$^+$ T cells express α7 nicotinic ACh receptor (*Chrna7*)
- ChAT$^+$ B cells support IL-6 production by Kupffer cells while limiting IFNγ from CD8$^+$ T cells
- Two ACh-based regulatory axes promote hepatocyte proliferation after liver injury

Authors

Nastaran Fazel Modares, Liam D. Hendrikse, Logan K. Smith, ..., Woo-Yong Lee, Paul Kubes, Tak W. Mak

Correspondence

tak.mak@uhn.ca

In brief

Liver regeneration (LR) is essential for recovery from acute trauma, cancer surgery, or transplantation. Fazel Modares et al. find that mouse LR after injury requires ChAT$^+$ B cells synthesizing acetylcholine (ACh) and Kupffer cells and hepatic CD8$^+$ T cells expressing α7 nicotinic ACh receptor (*Chrna7*). ChAT$^+$ B cells drive Kupffer cell IL-6 secretion and reduce CD8$^+$ T cell IFNγ.

Modares et al., 2025, Immunity *58*, 1201–1216
May 13, 2025
https://doi.org/10.1016/j.immuni.2025.04.002

CellPress

Immunity

CellPress
OPEN ACCESS

Article

B cell-derived acetylcholine promotes liver regeneration by regulating Kupffer cell and hepatic CD8$^+$ T cell function

Nastaran Fazel Modares,[1] Liam D. Hendrikse,[1] Logan K. Smith,[1] Michael St. Paul,[1] Jillian Haight,[1] Ping Luo,[1] Shaofeng Liu,[1] Jerome Fortin,[2] Frances K. Tong,[1] Andrew C. Wakeham,[1] Soode Moghadas Jafari,[1] Chunxing Zheng,[3] Mackenzie Buckland,[1] Robert Flick,[7] Jennifer Silvester,[1] Thorsten Berger,[1] Troy Ketela,[1] Simone Helke,[1] Erica Foffi,[1] Raheleh Niavarani,[1] Ryan Mcwilliam,[1] Mary E. Saunders,[1] Isabelle Colonna,[1] Bruna Araujo David,[4,5] Tashi Rastogi,[4,5] Woo-Yong Lee,[6] Paul Kubes,[4,5,6] and Tak W. Mak[1,3,8,9,10,*]

[1]Princess Margaret Cancer Centre, University Health Network, Toronto, ON, Canada
[2]Department of Neurology and Neurosurgery, McGill University, Montreal, QC, Canada
[3]Centre for Oncology and Immunology, Hong Kong Science Park, Hong Kong SAR, China
[4]Calvin Phoebe & Joan Snyder Institute for Chronic Diseases, Cumming School of Medicine, University of Calgary, Calgary, AB T2N 4N1, Canada
[5]Department of Physiology and Pharmacology Cumming School of Medicine, University of Calgary, Calgary, AB T2N 4N1, Canada
[6]Department of Biomedical and Molecular Science, Queen's University, Kingston, ON K7L 3N6, Canada
[7]Departments of Immunology and Medical Biophysics, University of Toronto, Toronto, ON, Canada
[8]Department of Pathology, School of Clinical Medicine, Li Ka Shing Faculty of Medicine, The University of Hong Kong, Queen Mary Hospital, Pokfulam, Hong Kong SAR, China
[9]Department of Chemical Engineering and Applied Chemistry, University of Toronto, Toronto, ON, Canada
[10]Lead contact
*Correspondence: tak.mak@uhn.ca
https://doi.org/10.1016/j.immuni.2025.04.002

SUMMARY

Liver regeneration (LR) is essential for recovery from acute trauma, cancer surgery, or transplantation. Neurotransmitters such as acetylcholine (ACh) play a role in LR by stimulating immune cells and augmenting hepatocyte proliferation, but the source of this ACh remains unclear. Here, we demonstrated that B cells expressing choline acetyltransferase (ChAT), which synthesizes ACh, were required for LR. Mice lacking ChAT$^+$ B cells subjected to partial hepatectomy (PHX) displayed greater mortality due to failed LR. Kupffer cells and hepatic CD8$^+$ T cells expressed the α7 nicotinic ACh receptor (nAChR), and LR was disrupted in mice lacking α7 nAChR. Mechanistically, B cell-derived ACh signaled through α7 nAChR to positively regulate the function of regenerative Kupffer cells and to control the activation of hepatic CD8$^+$ T cells to curtail harmful interferon-gamma (IFNγ) production. Our work offers insights into LR mechanisms that may point to therapies for liver damage.

INTRODUCTION

Liver tissue has an extraordinary potential to regenerate after injury, and liver regeneration (LR) is essential for a patient's recovery from acute trauma, cancer surgery, or transplantation. The capacity of the liver to regenerate is known to be mediated in part by nerves and neurotransmitters.[1–3] Nerve fibers have been shown to wrap around the hepatic artery, bile duct, and portal veins and have also been detected in direct contact with hepatocytes.[4,5] Neurotransmitters such as acetylcholine (ACh) play a role in LR by stimulating immune cells such as Kupffer cells[6–8] and by augmenting hepatocyte proliferation.[9–11] However, given that the liver is primarily innervated by sympathetic nerves, which produce norepinephrine (NE),[9,10] and not by parasympathetic nerves,[12–14] the source of this ACh promoting LR has remained unclear.

Recent evidence has identified lymphocytes as a critical source of ACh in various tissues, including the liver.[15,16] These T and B cell subsets express choline acetyltransferase (ChAT), the enzyme that catalyzes the conversion of choline and acetyl CoA into ACh. T cell-derived ACh is important for clearing viral infections[15] and for immunosurveillance[16] but can also mediate deleterious autoimmune responses.[17] Subsets of B cells expressing ChAT diminish neutrophil recruitment in mouse peritoneum during sterile endotoxemia and do so independently of the vagus nerve.[18] Thus, ACh-producing lymphocytes have far-reaching functions that extend beyond those of traditional neuronal circuits.

Among the various types of immune cells, Kupffer cells are thought to be particularly important for LR because of their production of hepatocyte mitogens such as interleukin-6 (IL-6) and tumor necrosis factor alpha (TNF-α).[19] B cells are also crucial for this process because B cell-deficient mice fail to regenerate their livers after partial hepatectomy (PHX).[20,21] Previous evidence suggested that B cells might support LR by producing cytokines and pro-angiogenic factors[22] or by maintaining IL-6-producing cells.[20] The tantalizing possibility that B cells might instead be the source of ACh required for functional LR prompted us to undertake this study.

Here, we report that B cells expressing ChAT (ChAT$^+$ B cells) were indeed induced during LR subsequent to 70% PHX in mice. This B cell-derived ACh was critical for hepatic regeneration, as mice lacking ChAT$^+$ B cells were unable to restore liver function. Furthermore, we demonstrated that mice deficient in nicotinic ACh receptor α7 (α7 nAChR; encoded by *Chrna7*), which was expressed by both Kupffer cells and T cells, also exhibited impaired LR following PHX. Mechanistically, our data support the hypothesis that hepatic CD8$^+$ T cells produced more interferon-gamma (IFNγ), and Kupffer cells produced less IL-6, in the absence of ChAT$^+$ B cells, phenotypes that were recapitulated in mice deficient for α7 nAChR. Our work suggests a mechanism in which B cell-derived ACh signals through α7 nAChR both to positively regulate the function of regenerative Kupffer cells and to control the activation of hepatic CD8$^+$ T cells so as to curtail harmful IFNγ production. This multifaceted, non-neuronal, ACh-mediated regulatory circuit appears to be essential for ensuring proper LR after acute injury.

RESULTS

Transcriptionally distinct ChAT$^+$ B cells are elevated during and required for LR

To elucidate the role of ChAT during LR, we utilized reporter mice expressing green fluorescent protein (GFP) under the control of the *Chat* promoter (ChAT-GFP mice). At 4 h post-PHX, ChAT was detected in both B cells and CD4$^+$ T cells (Figures 1A and S1A), but not in CD8$^+$ T cells (Figure S1B), in livers of these mice. However, only ChAT$^+$ B cells exhibited a significant increase in cell numbers in response to PHX (Figure 1B). We next endeavored to determine the source of these hepatic ChAT$^+$ B cells. Because the spleen is a reservoir of B cells and contributes substantially to LR,[20] we analyzed splenectomized ChAT-GFP mice at 4 h post-PHX. We observed only a minor decrease in the number of ChAT$^+$ B cells in the regenerating liver (Figure 1C), suggesting that the spleen is not a major source of hepatic ChAT$^+$ B cells. This result prompted us to dig deeper into the phenotype of ChAT$^+$ B cells.

At steady state, B cells resident in normal mouse livers are predominantly B-1 cells, which bear a clonal, semi-public, and predominantly immunoglobulin M (IgM) B cell receptor (BCR) repertoire.[23,24] We performed bulk RNA sequencing on GFP$^+$ and GFP$^-$ B cells (CD19$^+$B220$^+$) isolated from ChAT-GFP mice at 4 h post-sham surgery or PHX. Distinct transcriptional clustering was observed, with significant elevations of *Chat* and the ACh efflux pump *Slc18a3* expression in GFP$^+$ B cells (Figures 1D, S1C, and S1D). We used the TRUST4[23] algorithm to reconstruct BCR repertoires and found that post-PHX ChAT$^+$ B cells were substantially more clonal than ChAT$^-$ B cells (Figure S2A) and enriched for IgM BCRs (Figures 1E, S2B, and S2C). Public IgM BCRs were expanded among ChAT$^+$ B cells in 4/6 PHX mice and in 2/6 sham mice (Figure S2D), consistent with B-1 cells inducing ChAT expression in response to PHX. While these public IgM BCRs represented the dominant ChAT$^+$ B cell clone in several samples, most of the ChAT$^+$ B cell repertoire was private (Figure S2E), and expansion of non-IgM BCRs was restricted to PHX mice (Figure S2F).

Although phenotypic characterization by flow cytometry confirmed that hepatic B-1 cells induce ChAT following PHX, most ChAT$^+$ B cells in PHX liver were follicular B-2 cells, suggesting that ChAT$^+$ B cells could also be recruited from the circulation in response to PHX (Figures S3A–S3H). We did not observe significant differences in proliferation between ChAT$^+$ B cells and ChAT$^-$ B cells at 4 h post-PHX (Figure S3I). In one PHX mouse, ChAT was retained after class switching, suggesting the persistence of ChAT expression in daughter cells (Figure 1F). At 24 h post-PHX, follicular B-2 cells remained the dominant ChAT$^+$ phenotype, but their frequency had markedly decreased (Figures S3J and S3K). Collectively, these results suggest that induction of ChAT in liver-resident B cells, rather than proliferation of existing ChAT$^+$ B cells, is a very early response to liver damage. This response can be further augmented by the recruitment of ChAT$^+$ follicular B cells from circulation.

B-1 cells are primed for rapid response to insult, and the most prevalent public BCRs in our ChAT$^+$ B cells had similar sequences (Figure 1G), which led us to examine how ChAT is induced in B cells. Norepinephrine (NE) induces ChAT in T cells,[25] and lipopolysacchride (LPS), whose levels increase in the gut and liver following PHX,[26,27] induces ChAT in B cells.[18] We stimulated splenic B cells from our reporter mice *in vitro* with various concentrations of NE, LPS, or anti-IgM antibody and observed significant ChAT induction in each case (Figure S3L and S3M). Notably, combining LPS and NE did not have a synergistic effect (Figure 1H), suggesting that distinct LPS-reactive and NE-reactive B cells exist and that both NE and LPS can induce ChAT in B cells.

To delve further into the phenotype of ChAT$^+$ B cells responding to PHX, we delineated transcription patterns of ChAT$^+$ vs. ChAT$^-$ B cells isolated from reporter mice at 4 h post-PHX. ChAT$^+$ B cells exhibited marked transcriptional changes in response to PHX that affected pathways related to hypoxia-inducible factor 1 (HIF-1), phosphatidylinositol 3-kinase and protein kinase B (PI3K)-Akt signaling, and axon guidance, implying the activation of hypoxia responses and a role in neuro-immune communication (Figures S4A–S4C; see also Tables S1–S4). By contrast, ChAT$^-$ B cells were enriched for expression of genes related to antigen processing and presentation (Figures S4A–S4C; see also Table S4).

To investigate genetically whether ChAT$^+$ B cells or ChAT$^+$ T cells are essential for LR, we created two transgenic mouse strains in which either B lineage or T lineage cells specifically lacked ChAT expression and thus ACh production (ChAT$^{flox;Mb1\text{-}Cre}$ and ChAT$^{flox;Cd4\text{-}Cre}$ mice, respectively).[15,18] The concentration of hepatic ACh was increased in whole livers of control ChAT^{flox} mice at 4 h post-PHX (Figure S4D). Both ChAT^{flox} and ChAT$^{flox;Cd4\text{-}Cre}$ mice exhibited robust survival at day 12 post-PHX (Figure S4E). By contrast, ChAT$^{flox;Mb1\text{-}Cre}$

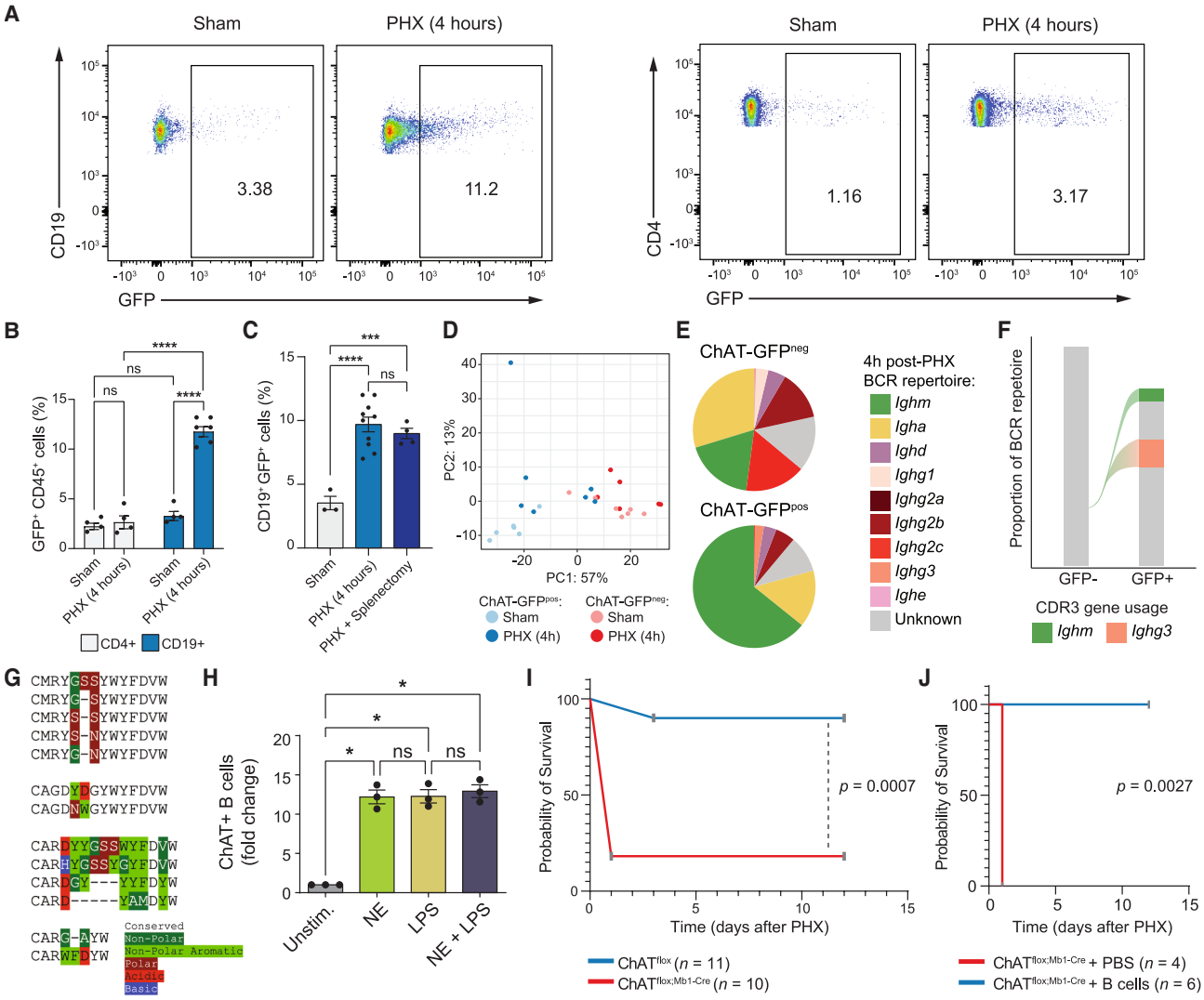

Figure 1. Transcriptionally distinct hepatic ChAT$^+$ B cells are elevated in response to 70% PHX

(A and B) Representative flow cytometric plots (A) and quantitation (B) of ChAT-GFP expression by hepatic B cells isolated from ChAT-GFP reporter mice ($n = 6$) at 4 h post-PHX, hepatic T cells isolated from ChAT-GFP reporter mice ($n = 4$) at 4 h post-PHX, or ChAT-GFP reporter mice ($n = 4$) subjected to sham surgery. ****$p <$ 0.0001 by unpaired t test. ns, not significant.

(C) Percentage of CD19$^+$ ChAT-GFP cells in livers of ChAT-GFP reporter mice subjected to sham surgery ($n = 3$) or to PHX alone ($n = 10$), or to splenectomy at 4 h post-PHX ($n = 4$). ****$p = 0.0001$, ***$p = 0.0008$ by one-way ANOVA.

(D) Principal-component analysis (PCA) analysis using VST-transformed bulk RNA sequencing expression data obtained from ChAT-GFP reporter mice at 4 h post-PHX or sham surgery. Samples were primarily separated by ChAT (GFP) positivity.

(E) Pie charts representing the B cell receptor (BCR) heavy-chain repertoire of ChAT$^+$ and ChAT$^-$ B cells isolated from ChAT-GFP reporter mice at 4 h post-PHX. Sections are colored by constant gene usage for each CDR3 sequence.

(F) Alluvial plot for mouse #173 showing an *Ighm* CDR3 sequence that was expanded in ChAT$^+$ B cells and also class-switched into an *Ighg3* BCR.

(G) Amino acid sequences of the CDR3 regions of public BCRs from ChAT-GFP$^+$ B cells. Sequences are grouped based on similarity. Residues that are conserved in each group are not highlighted. Non-conserved residues are highlighted as follows: red, acidic residues; blue, basic residues; brown, polar residues; dark green, non-polar residues; and light green, non-polar aromatic residues.

(H) Quantitation of fold change in ChAT$^+$ B cell numbers in cultures of total splenic B cells that were isolated from ChAT-GFP mice and left unstimulated or treated *in vitro* for 4 h with LPS 20 ng/mL, NE (100 ng/mL), or both. **$p = 0.0168$ by one-way ANOVA.

(I) Kaplan-Meier survival curves over 12 days of ChAT$^{flox;Mb1\text{-}Cre}$ ($n = 10$) and ChAT^{flox} mice ($n = 11$) mice after 70% PHX. $p = 0.0007$ by log-rank (Mantel-Cox) test.

(J) Kaplan-Meier survival curves over 12 days of ChAT$^{flox;Mb1\text{-}Cre}$ mice ($n = 6$) that received adoptive transfer of two doses of 10×10^6 WT CD45.1$^+$ B cells: one dose administered intravenous (i.v.) at 48 h prior to 70% PHX, and the other dose administered intraperitoneal (i.p.) prior to PHX. Control ChAT$^{flox;Mb1\text{-}Cre}$ mice ($n = 4$) received parallel administrations of PBS. **$p = 0.0027$ by log-rank (Mantel-Cox) test. For all figure panels, where appropriate, data are the mean ± SEM and representative of at least 3 independent experiments unless otherwise indicated.

See also Figures S1–S4 and Tables S1, S2, S3, and S4.

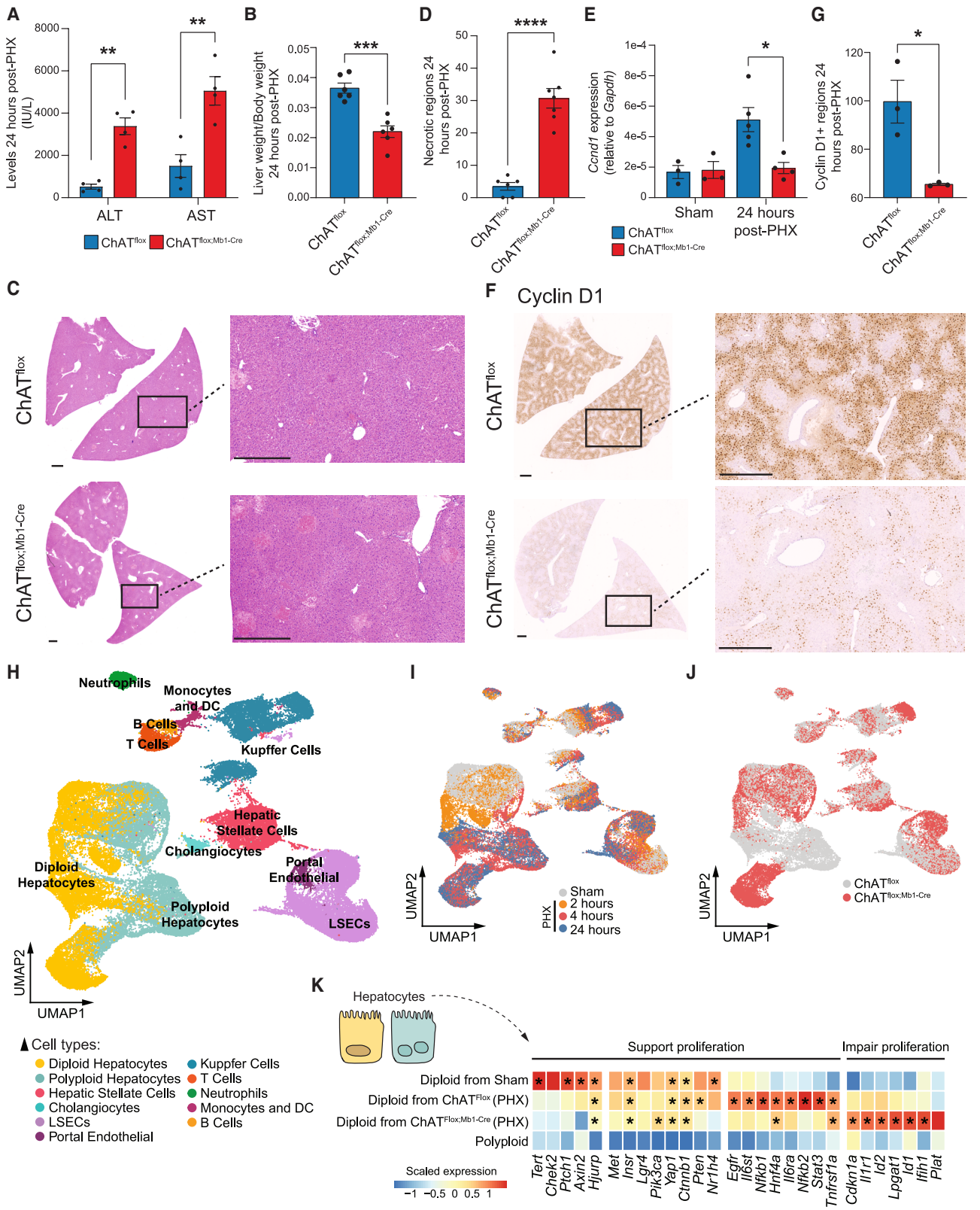

Figure 2. Impaired hepatocyte proliferation in the absence of ChAT^{+} B cells after 70% PHX

(A) Activity levels of ALT and AST enzymes in ChAT^{flox} and ChAT$^{flox;Mb1\text{-}Cre}$ mice (n = 4/group) at 24 h post-PHX. **$p \leq 0.01$ by two-way ANOVA.

(B) Liver weight-to-body weight ratios of ChAT^{flox} and ChAT$^{flox;Mb1\text{-}Cre}$ mice (n = 6/group) at 24 h post-PHX. ***$p = 0.0002$ by unpaired t test.

(legend continued on next page)

mice subjected to 70% PHX died quickly, typically reaching the humane endpoint by 24 h post-PHX (Figure 1I). The survival of these ChAT$^{flox;Mb1\text{-}Cre}$ mice could be rescued by adoptive transfer of wild-type (WT) CD45.1^{+} B cells (Figure 1J).

Taken together, these data indicate that it is B cells that are the rapid responders to acute liver injury and that they induce ChAT to produce the ACh required for successful LR.

Hepatocyte proliferation is impaired in the absence of ChAT^{+} B cells after 70% PHX

To confirm that the greater mortality of ChAT$^{flox;Mb1\text{-}Cre}$ PHX mice was due to their lack of ChAT^{+} B cells, we examined several factors routinely used to assess liver health. At 24 h post-PHX, ChAT$^{flox;Mb1\text{-}Cre}$ mice exhibited elevated activities of the liver damage indicators alanine transaminase (ALT) and aspartate aminotransferase (AST) (Figure 2A) as well as a decreased liver weight-to-body weight ratio (Figure 2B). ChAT$^{flox;Mb1\text{-}Cre}$ mice also displayed more necrotic areas in the liver at 24 h post-PHX compared with ChAT^{flox} mice (Figures 2C and 2D). Thus, a failure to regenerate a healthy liver likely underlies the mortality of PHX mice lacking ChAT^{+} B cells.

To understand why LR failed in these animals, we evaluated hepatocyte proliferation in the presence or absence of ChAT^{+} B cells. At 24 h post-PHX of ChAT^{flox} and ChAT$^{flox;Mb1\text{-}Cre}$ mice, we observed reduced mRNA expression of the hepatocyte proliferation marker *Ccnd1* in the mutant (Figure 2E), as well as decreased Cyclin D1 protein in whole liver (Figures 2F and 2G). Next, we conducted single-cell RNA sequencing (scRNA-seq) of hepatic cells isolated from ChAT^{flox} and ChAT$^{flox;Mb1\text{-}Cre}$ mice at 2, 4, and 24 h post-PHX or sham surgery. We identified many of the expected liver cell populations, including hepatic stellate cells, Kupffer cells, liver sinusoidal endothelial cells (LSECs), B and T cells, neutrophils, monocytes, and cholangiocytes (Figures 2H–2J, S5A, and S5B; see also Table S5). Diploid and polyploid hepatocytes, both of which are present in normal intact liver but which differ in their RNA content,[28,29] were also identified (Figures 2H–2J). Following acute liver injury (such as PHX), diploid hepatocytes, but not polyploid hepatocytes, undergo rapid proliferation.[30] When we examined our scRNA-seq data for expression patterns of genes involved in hepatocyte proliferation, we found (1) increased expression of many proliferation-supporting genes in diploid hepatocytes from ChAT^{flox} mice post-PHX, (2) elevated expression of genes associated with impaired hepatocyte proliferation in diploid hepatocytes from ChAT$^{flox;Mb1\text{-}Cre}$ mice post-PHX, and (3) reduced expression of proliferation genes in polyploid hepatocytes overall (Figure 2K). Among the hepatocyte proliferation genes that were decreased in the absence of ChAT^{+} B cells were those encoding IL-6 receptors (*Il6ra* and *Il6st*) and their downstream targets signal transducer and activator of transcription 3 (*Stat3*), *Nfkb1*, and *Nkfb2*[7,31–35] (Figure 2K), suggesting that IL-6 signaling is deficient in the absence of ChAT^{+} B cells.

Collectively, these data bolster our hypothesis that the higher mortality rate of ChAT$^{flox;Mb1cre}$ mice post-PHX is linked to impaired hepatocyte proliferation leading to failed LR.

Phenotypic alterations of Kupffer cells and hepatic CD8^{+} T cells are evident in the absence of ChAT^{+} B cells

Kupffer cells are important for LR because they produce IL-6, a necessary mitogen for hepatocyte proliferation following liver damage.[19,36] Thus, a deficiency in IL-6 signaling to hepatocytes in the absence of ChAT^{+} B cells might implicate Kupffer cells as a target of B cell-derived ACh. We performed a sub-clustering and trajectory analysis and found that Kupffer cells isolated from ChAT^{flox} vs. ChAT$^{flox;Mb1\text{-}Cre}$ mice at 24 h post-PHX had different fates (Figures 3A and S5C–S5E; see also Tables S6 and S7). In the absence of ChAT^{+} B cells, Kupffer cells displayed an immunosuppressive phenotype at 24 h post-PHX, expressing genes such as *Il10*, *Ms4a8a*, *Ms4a4a*, *Hmox1*, and *Ripk3* (Figures 3B, 3C, and S5F; see also Tables S6 and S7). IL-10 is known to suppress TNF and IL-6 expression by Kupffer cells.[37,38] In line with this finding, we observed a significant decrease in the proportion of IL-6^{+} Kupffer cells as well as a marked reduction in serum IL-6 in ChAT$^{flox;Mb1\text{-}Cre}$ mice compared with ChAT^{flox} controls at 24 h post-PHX (Figures 3D and 3E). ChAT^{flox} mice treated prior to PHX with clodronate liposomes to deplete Kupffer cells[39] exhibited a higher mortality rate compared with untreated ChAT^{flox} mice (Figure 3F), an effect reversed by treating the mice with exogenous IL-6 at 48 h after clodronate liposome administration (Figure 3F). Thus, to achieve normal LR, it seems that ChAT^{+} B cells must stimulate Kupffer cells to produce sufficient IL-6 to ensure adequate hepatocyte proliferation.

T cells also play a role in recovery from liver damage because mice deficient in T cells display impaired LR post-PHX.[21] As detailed in the spatially resolved scRNA-seq atlas of WT mouse LR compiled by Xu et al.,[40] livers of WT mice responding to PHX show much-reduced numbers of hepatocytes responding to CD8^{+} T cell-derived IFNγ compared with homeostatic WT liver.[40]

(C) Representative images at 2 magnifications of H&E-stained liver sections taken from ChAT^{flox} (n = 6) and ChAT$^{flox;Mb1\text{-}Cre}$ (n = 7) mice at 24 h post-PHX. Scale bars, 500 μm.

(D) Quantitation of necrotic areas in the livers in (C) using Fiji software. ****$p \leq 0.0001$ by unpaired t test.

(E) qPCR determination of relative mRNA expression levels of *Ccnd1* in whole livers isolated from ChAT^{flox} (n = 5) and ChAT$^{flox;Mb1\text{-}Cre}$ (n = 4) mice at 24 h post-PHX or sham surgery (n = 3). *p = 0.0127 by unpaired t test.

(F) Representative images at 2 magnifications of liver sections from ChAT^{flox} and ChAT$^{flox;Mb1\text{-}Cre}$ mice (n = 3/group) stained with anti-cyclin D1 antibody. Scale bars, 500 μm.

(G) Quantitation of cyclin D1^{+} areas in the livers in (F) using Fiji software. *p = 0.0182 by unpaired t test.

(H–J) UMAP embedding of 57,436 single cells isolated from the livers of ChAT^{flox} and ChAT$^{flox;Mb1\text{-}Cre}$ mice following PHX or sham surgery. Cells are colored by annotated cell types (H), time post-PHX (I), or mouse genotype (J).

(K) Heatmap showing expression of genes known to be involved in supporting or impairing hepatocyte proliferation in diploid and polyploid hepatocytes (as in H), isolated from the livers of ChAT^{flox} or ChAT$^{flox;Mb1\text{-}Cre}$ mice (as in J), following sham or PHX surgery (as in I). Differential expression (DE) analysis between groups was performed using the false discovery rate (FDR) correction. Significant DE genes (FDR < 0.05) are indicated with an asterisk (*).

See also Figures S5A and S5B. See also Table S5.

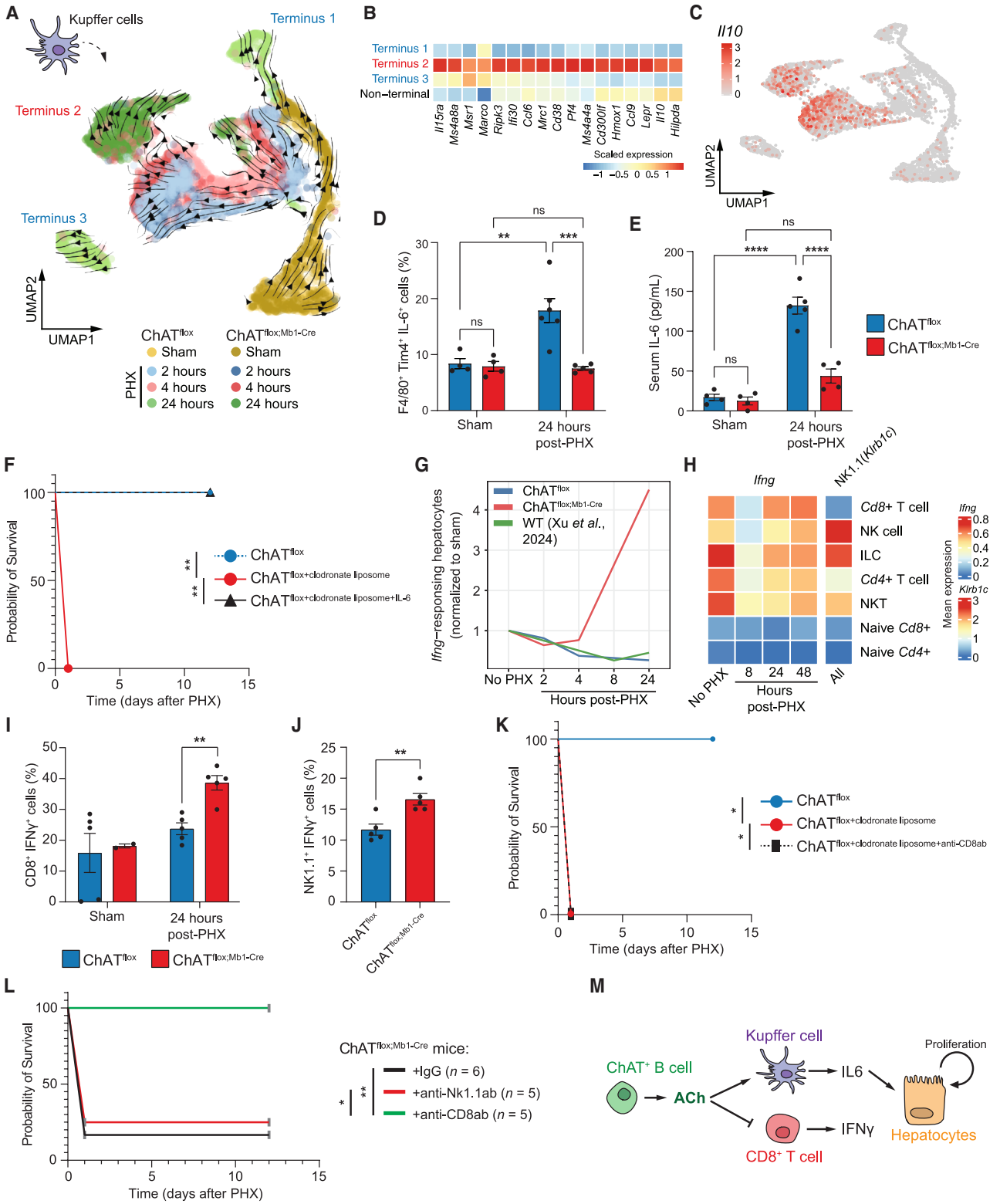

Figure 3. Phenotypic alterations of Kupffer cells and hepatic CD8⁺ T cells occur in the absence of ChAT⁺ B cells

(A) Pseudotime ordering of Kupffer cells from livers of ChAT^{flox} and ChAT$^{flox;Mb1\text{-}Cre}$ mice projected onto a UMAP embedding. Arrows indicate the direction of phenotypic changes. Data are largely consistent with the time point (cell color) at which the cells were isolated. Kupffer cells were sub-clustered from the scRNA-seq data in Figure 2. Pseudotime ordering was determined using Slingshot, and CellRank was used to compute global ordering.

(legend continued on next page)

Given that IFNγ impedes hepatocyte proliferation,[41,42] we hypothesized that ChAT$^+$ B cells might negatively regulate IFNγ production by CD8$^+$ T cells. Indeed, we found decreased numbers of IFNγ-responding hepatocytes (defined by their expression of *Rsad2*, *Ifit1*, and *Oasl1*) in our control ChAT^{flox} mice post-PHX (Figure 3G). In the absence of ChAT$^+$ B cells, we observed a 4-fold elevation in the number of IFNγ-responding hepatocytes by 24 h post-PHX, accompanied by an increased proportion of hepatocytes expressing IFNγ receptor genes (*Ifngr1* and *Ifngr2*) (Figure S5G). However, Xu et al.[40] have shown that not only CD8$^+$ T cells but also natural killer (NK), natural killer T (NKT) cells, innate lymphoid cells (ILCs), and CD4$^+$ T cells express *Ifng* post-PHX (Figures 3H, S5H, and S5I). In our hands, while *Cd8a* was expressed by both CD8$^+$ T cells and NKT cells, expression of *Klrb1c* (encoding NK1.1) segregated CD8$^+$ T cells from other *Ifng*$^+$ cell types (Figures 3H and S5I).

To explore the above observations genetically, we isolated various lymphoid cell types from ChAT^{flox} and ChAT$^{flox;Mb1\text{-}Cre}$ livers at 24 h post-PHX and quantified their IFNγ production using flow cytometry. Without ChAT$^+$ B cells, CD8$^+$ cells, and NK1.1$^+$ cells produced significantly more IFNγ than controls at 24 h post-PHX (Figures 3I, 3J, and S5J). We next depleted Kupffer cells and/or CD8$^+$ T cells in ChAT^{flox} mice using clodronate liposomes and/or anti-CD8 antibody, respectively. A lack of Kupffer cells, either alone or together with CD8$^+$ T cell depletion, sharply increased the mortality rate of ChAT^{flox} PHX mice (Figure 3K). We then utilized anti-CD8 or anti-NK1.1 antibodies to conduct *in vivo* depletion experiments targeting CD8$^+$ T cells or NK1.1$^+$ cells, respectively, in ChAT$^{flox;Mb1\text{-}Cre}$ PHX mice. Depletion of CD8$^+$ T cells, but not NK1.1$^+$ cells, led to reduced liver IFNγ production that allowed normal survival of ChAT$^{flox;Mb1\text{-}Cre}$ mice post-PHX (Figures 3L and S5K). Thus, without ChAT$^+$ B cells, hepatic CD8$^+$ T cells exhibit heightened production of IFNγ that impedes LR after PHX.

Taken together, these results suggest that ChAT$^+$ B cells play a dual role in orchestrating LR by (1) inducing IL-6 production by Kupffer cells and (2) limiting the activation of effector CD8$^+$ T cells and thereby reducing toxic IFNγ production (Figure 3M). ChAT$^+$ B cells may therefore be crucial for modulating immune responses and hepatocyte proliferation during LR.

LR is impaired in α7 nAChR knockout mice after 70% PHX

ACh signals to immune cells via acetylcholine receptors (AChRs), with previous studies demonstrating that α7 nAChR is expressed on macrophages during the anti-inflammatory reflex[43–46] and on T cells.[47] To infer which AChR(s) are used by Kupffer cells and CD8$^+$ T cells to respond to B cell-derived ACh, we accessed data from the WT mouse LR atlas of Xu et al.[40] and saw that the number of *Chat*$^+$ spatial spots rose significantly at 8 h post-PHX (Figure 4A). Furthermore, these *Chat*$^+$ spots were enriched for *Cd79a*, suggesting the presence of B cells (Figure 4B). We performed spatially resolved deconvolution using time-matched scRNA-seq data (also from Xu et al.,[40] Figure S5H) and determined that, among all AChR genes analyzed, only *Chrna7* expression (encoding α7 nAChR) was specifically co-localized with B cells, CD8$^+$ T cells, and Kupffer cells (Figures 4C, 4D, S6A, and S6B), and only at 8 h post-PHX (Figure 4C). Regions of overlapping *Chat* and *Chrna7* expression density were enriched for expression of B cell genes (*Iglc1*, *Ighm*, and *Jchain*) (Figures 4E, S6C, and S6D), supporting the co-localization of *Chat*$^+$ B cells with *Chrna7*$^+$ cells. Intravital microscopy of WT mouse liver at 4 h post-PHX further demonstrated the interaction of B cells, CD8$^+$ T cells, and Kupffer cells (Figures S6E and S6F). Lastly, using qPCR and flow cytometry, we confirmed that WT Kupffer and hepatic CD8$^+$ T cells both express α7 nAChR (Figures 4F and S6G).

We next undertook studies of α7 nAChR knockout (α7-KO) mice in which all immune cell types would lack *Chrna7* expression. As expected, mRNA and protein levels of α7 nAChR were reduced when these cell types were isolated from naive α7-KO mice (Figures 4F and S6G). We then subjected α7-KO mice to 70% PHX and observed a significantly higher mortality rate compared with controls (Figure 4G). At 24 h post-PHX, α7-KO mice exhibited elevated ALT and AST activities (Figure 4H), a

(B) Heatmap showing expression of selected genes that correlated robustly with one of the three indicated terminal fates identified in (A). Terminus 2 corresponds to a Kupffer cell fate primarily comprised of cells isolated from livers of ChAT$^{flox;Mb1\text{-}Cre}$ mice at 4 and 24 h post-PHX.
(C) UMAP plot showing that *Il10* expression is robustly enriched along the Terminus 2 Kupffer cell fate.
(D) Quantitation of flow cytometric determination of IL-6 in F4/80$^+$ Tim4$^+$ Kupffer cells isolated from livers of ChAT^{flox} and ChAT$^{flox;Mb1\text{-}Cre}$ mice at 24 h after PHX or sham surgery. ***$p \leq 0.001$ and **$p \leq 0.01$ by two-way ANOVA.
(E) Protein levels of IL-6 as measured by ELISA in ChAT^{flox} and ChAT$^{flox;Mb1\text{-}Cre}$ mice at 24 h post-PHX. ****$p \leq 0.0001$ by two-way ANOVA.
(F) Kaplan-Meier survival curves over 12 days of ChAT^{flox} mice subjected to PHX ($n = 3$), ChAT^{flox} mice depleted of Kupffer cells by treatment with clodronate liposomes prior to PHX ($n = 4$), and ChAT^{flox} mice treated with clodronate liposomes + IL-6 prior to PHX ($n = 5$). **$p = 0.0067$ by log-rank test.
(G) Number of *Ifng*-responding *Rsad2*$^+$, *Ifit1*$^+$, and/or *Oasl1*$^+$ hepatocytes in livers of ChAT^{flox} and ChAT$^{flox;Mb1\text{-}Cre}$ mice at the indicated time points post-PHX as compared with atlas data published by Xu et al.[40] for WT mice post-PHX. Values were normalized to each group's sham starting point.
(H) Heatmap of *Ifng* and *Klrb1c* expression in the indicated immune cell subsets as constructed from published atlas data.[40]
(I) Quantitation of flow cytometric determination of IFNγ production by hepatic CD8$^+$ T cells isolated from ChAT^{flox} and ChAT$^{flox;Mb1\text{-}Cre}$ mice ($n = 5$) at 24 h post-PHX or sham surgery. **$p = 0.0012$ by unpaired t test.
(J) Quantitation of flow cytometric determination of IFNγ production by hepatic NK1.1$^+$ cells isolated from ChAT^{flox} and ChAT$^{flox;Mb1\text{-}Cre}$ mice ($n = 5$) at 24 h post-PHX or sham treatment. **$p = 0.0051$ by unpaired t test.
(K) Kaplan-Meier survival curves over 12 days of ChAT^{flox} mice subjected to PHX ($n = 3$), ChAT^{flox} mice depleted of Kupffer cells by treatment with clodronate liposomes prior to PHX ($n = 4$), and ChAT^{flox} mice treated clodronate liposomes + anti-CD8 antibody prior to PHX ($n = 3$). *$p = 0.0253$ by log-rank test.
(L) Kaplan-Meier survival curves over 12 days of ChAT$^{flox;Mb1\text{-}Cre}$ mice that were treated with anti-CD8 antibody (ab) ($n = 5$) or anti-NK1.1 antibody ($n = 5$) on days 1 and 3 prior to PHX. Control ChAT$^{flox;Mb1\text{-}Cre}$ mice ($n = 6$) received control IgG prior to PHX. *$p = 0.0178$ by log-rank (Mantel-Cox) test.
(M) Schematic representation of the proposed interactions among ChAT$^+$ B cells producing ACh (green), Kupffer cells producing IL-6 (purple), and CD8$^+$ T cells producing IFNγ (red), and how these cytokines affect the proliferation of hepatocytes (yellow).
See also Figures S5C–S5K and Tables S6 and S7.

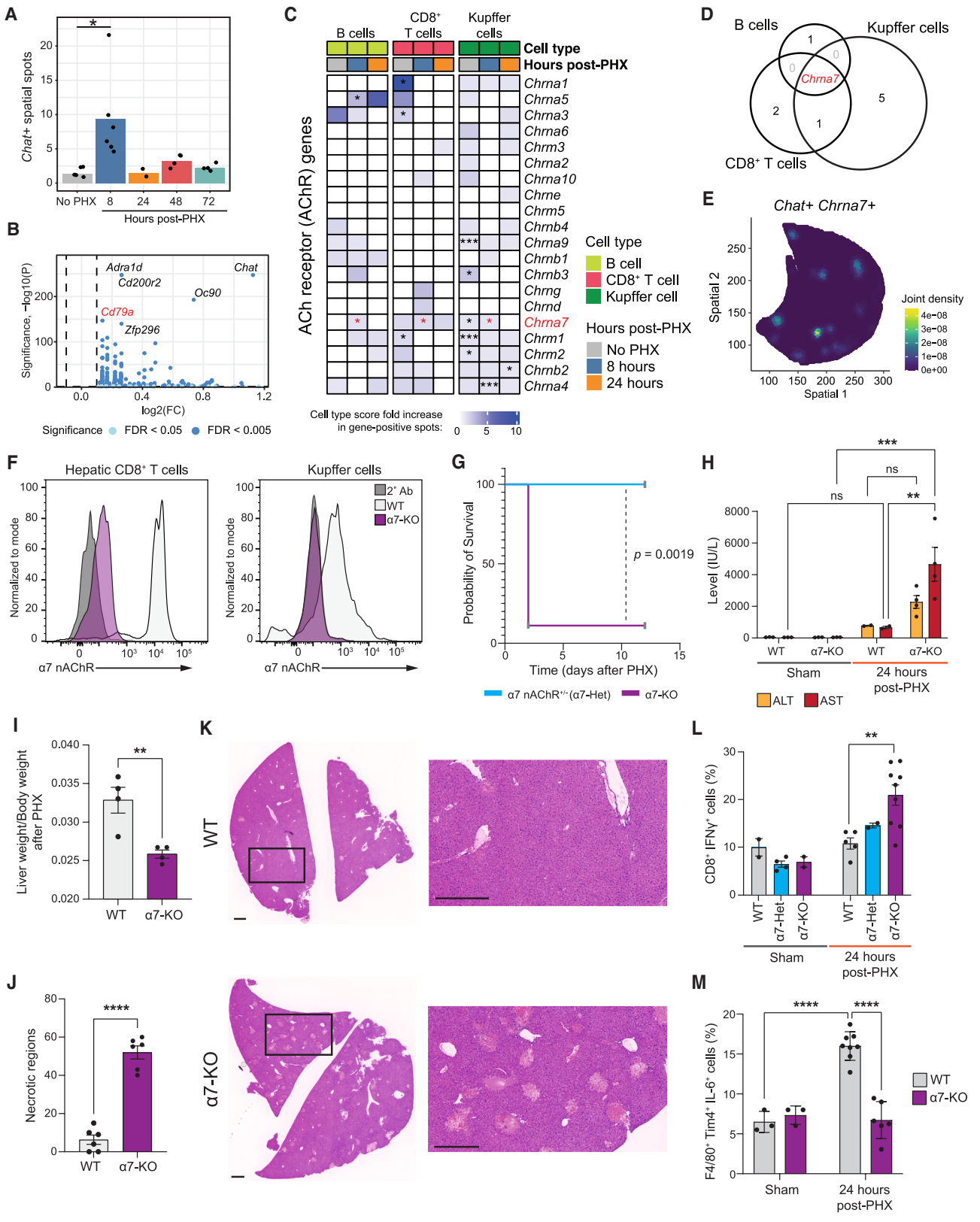

(legend on next page)

decreased liver weight-to-body weight ratio (Figure 4I), and increased numbers of hepatic necrotic regions compared with WT mice (Figures 4J and 4K). Compared with controls, $CD8^+$ T cells from α7-KO mice produced more IFNγ at 24 h post-PHX, whereas Kupffer cells from the same livers secreted less IL-6 (Figures 4L and 4M).

Thus, the genetic ablation of α7 nAChR and the B cell-specific deletion of ChAT have strikingly parallel effects on mouse survival, LR, and cytokine production by hepatic cell populations following PHX. These results therefore imply that $ChAT^+$ B cells signal to Kupffer cells and $CD8^+$ T cells through α7 nAChR during LR.

ACh exerts bi-axial regulation of LR through α7 nAChR

Having shown that α7 nAChR is indispensable for LR, we sought to determine if ACh/α7 nAChR signaling was directly linked to the altered phenotypes of $CD8^+$ T cells and Kupffer cells in $ChAT^{flox;Mb1\text{-}Cre}$ mice. We isolated $CD8^+$ T cells from livers of WT or α7-KO mice and activated them *in vitro* with Phorbol 12-myristate 13-acetate (PMA)/ionomycin (iono) in the presence or absence of 500 μM ACh plus 150 mM (final concentration) pyridostigmine (an acetylcholinesterase inhibitor that minimizes ACh degradation[49]). ACh treatment significantly reduced IFNγ expression by WT $CD8^+$ T cells but had no effect on α7-KO $CD8^+$ T cells (Figure 5A). This effect of ACh on the expression of IFNγ, as well as on the expression of the activation marker CD107a,[50] was dose-dependent in WT $CD8^+$ T cells but completely abolished in α7-KO $CD8^+$ T cells (Figures 5B and 5C). This *in vitro* demonstration that the direct stimulation of $CD8^+$ T cells by ACh decreases IFNγ production recapitulates our *in vivo* findings above.

To determine how ACh performs its role during LR, we built on previous evidence indicating that the AKT and mitogen-activated protein kinase (MAPK) signaling pathways can trigger T cell production of IFNγ.[51] We isolated $CD8^+$ cells from livers of WT and α7-KO mice, treated these cells *in vitro* with 500 μM ACh, and assessed the phosphorylation (activation) of AKT and extracellular signal-regulated kinase (ERK1/2). A significant reduction in the phosphorylation of both AKT and ERK1/2 occurred in ACh-treated WT $CD8^+$ T cells but not in ACh-treated α7-KO $CD8^+$ T cells (Figures 5D and 5E). Thus, ACh signaling through α7 nAChR may suppress AKT and MAPK signaling so as to reduce $CD8^+$ T cell activation and consequently IFNγ production.

To assess whether ACh/α7 nAChR signaling was also directly related to the altered phenotypes of Kupffer cells isolated from $ChAT^{flox;Mb1\text{-}Cre}$ mice, we used CRISPR technology to generate α7 nAChR KO in murine macrophage-like cell line (RAW 264.7 cells). We stimulated RAW 264.7^{wt} and RAW $264.7^{\alpha7ko}$ cells for 4 h with varying concentrations of ACh (in the presence of pyridostigmine[49]) and observed significant induction of IL-6 production in RAW 264.7^{wt} cells but not in RAW $264.7^{\alpha7ko}$ cells (Figure 5F). IL-6 is required for STAT3 activation in liver cells shortly after PHX, with IL-6-deficient mice showing a lack of STAT3 activation that is restored upon exogenous IL-6 administration.[52–54] We detected an increase in STAT3 phosphorylation in RAW 264.7^{wt} cells after ACh stimulation but not in RAW $264.7^{\alpha7ko}$ cells (Figure 5G), suggesting that ACh/α7 nAChR interaction is required for the IL-6 signaling driving STAT3 activation following PHX.

Our data above point to an unexpected dichotomous role in LR for $ChAT^+$ B cells. To elucidate the differential contributions of B cell/Kupffer cell and B cell/$CD8^+$ T cell interactions in this complex process, we performed adoptive transfer experiments. Adoptive transfer of WT $CD8^+$ T cells into α7-KO mice that then underwent PHX improved their survival, with 50% of mutant animals surviving to day 12 (Figure 5H). The examination of the Kupffer cell contribution was more challenging due to the technical difficulties associated with their isolation from mouse liver. However, bone marrow (BM)-derived monocytes adoptively transferred into a liver lacking resident Kupffer cells will differentiate into Kupffer cells.[55,56] We therefore isolated

Figure 4. LR is impaired in α7-KO mice after 70% PHX

(A) Quantitation of *Chat*$^+$ spatial spots as constructed from published atlas data[40] on sham-treated WT mice ($n = 5$), and WT mice at 8 ($n = 5$), 24 ($n = 4$), 48 ($n = 5$), or 72 ($n = 5$) h post-PHX. *$p = 0.0073$ by two-sided Wilcoxon rank sum test.

(B) Volcano plot showing significant differentially expressed genes in the *Chat*$^+$ spatial spots in (A). Significance was assessed using a two-sided Wilcoxon rank sum test with FDR correction.

(C) Heatmap showing fold change in the expression of the indicated AChR-encoding genes as constructed from published atlas data[40] on B cells, $CD8^+$ T cells, and Kupffer cells in WT mice at the indicated times post-PHX (results for all cell types are shown in Figure S6B). RCTD[48] was used to deconvolute spatial spot data with the annotated single-cell data from Xu et al.[40] Significance asterisks were overlaid. *$p < 0.05$, ***$p < 0.0005$ by two-sided Wilcoxon rank sum test. Blank, non-significant (ns).

(D) Venn diagram summarizing the *Chrna7* expression data in (C). At 8 h post-PHX, *Chrna7* was the only AChR gene showing a significant overlap between WT B cells, $CD8^+$ T cells, and Kupffer cells.

(E) Joint expression density of *Chat* and *Chrna7* as constructed from published atlas data[40] in a representative spatial sample from WT liver at 8 h post-PHX.

(F) Representative flow cytometric determinations of α7 nAChR protein in hepatic $CD8^+$ T cells and Kupffer cells isolated from WT and α7-KO mice ($n = 3$) at 24 h post-PHX.

(G) Kaplan-Meier survival curves over 12 days of α7-KO ($n = 9$) and control α7-heterozygous (het) ($n = 5$) mice after 70% PHX. $p = 0.0019$ by log-rank (Mantel-Cox) test.

(H) Activity levels of ALT and AST enzymes in WT ($n = 3$) and α7-KO ($n = 4$) mice at 24 h post-PHX or sham surgery. ***$p = 0.0004$, **$p = 0.74$, by two-way ANOVA.

(I) Liver weight-to-body weight ratios of α7-KO and WT mice ($n = 4$/group) at 24 h post-PHX. **$p = 0.0074$ by unpaired t test.

(J) Quantitation of necrotic areas in the livers in (K) using Fiji software. ****$p \leq 0.0001$ by unpaired t test.

(K) Representative images at 2 magnifications of H&E-stained liver sections from WT and α7-KO mice ($n = 6$/group) at 24 h post-PHX. Scale bars, 500 μm.

(L) Quantitation of flow cytometric determination of IFNγ production by hepatic $CD8^+$ T cells that were isolated from WT, α7-het, or α7-KO mice at 24 h after PHX (WT, $n = 5$; α7-het, $n = 2$; α7-KO, $n = 9$) or sham surgery (WT, $n = 2$; α7-het, $n = 4$; α7-KO, $n = 2$). **$p = 0.0056$ by one-way ANOVA.

(M) Quantitation of flow cytometric determination of IL-6 production by Kupffer cells that were isolated from WT or α7-KO mice at 24 h after PHX (WT, $n = 8$; α7-KO, $n = 6$), or sham surgery (WT, $n = 3$; α7-KO, $n = 3$). ****$p \leq 0.0001$ by two-way ANOVA.

See also Figure S6.

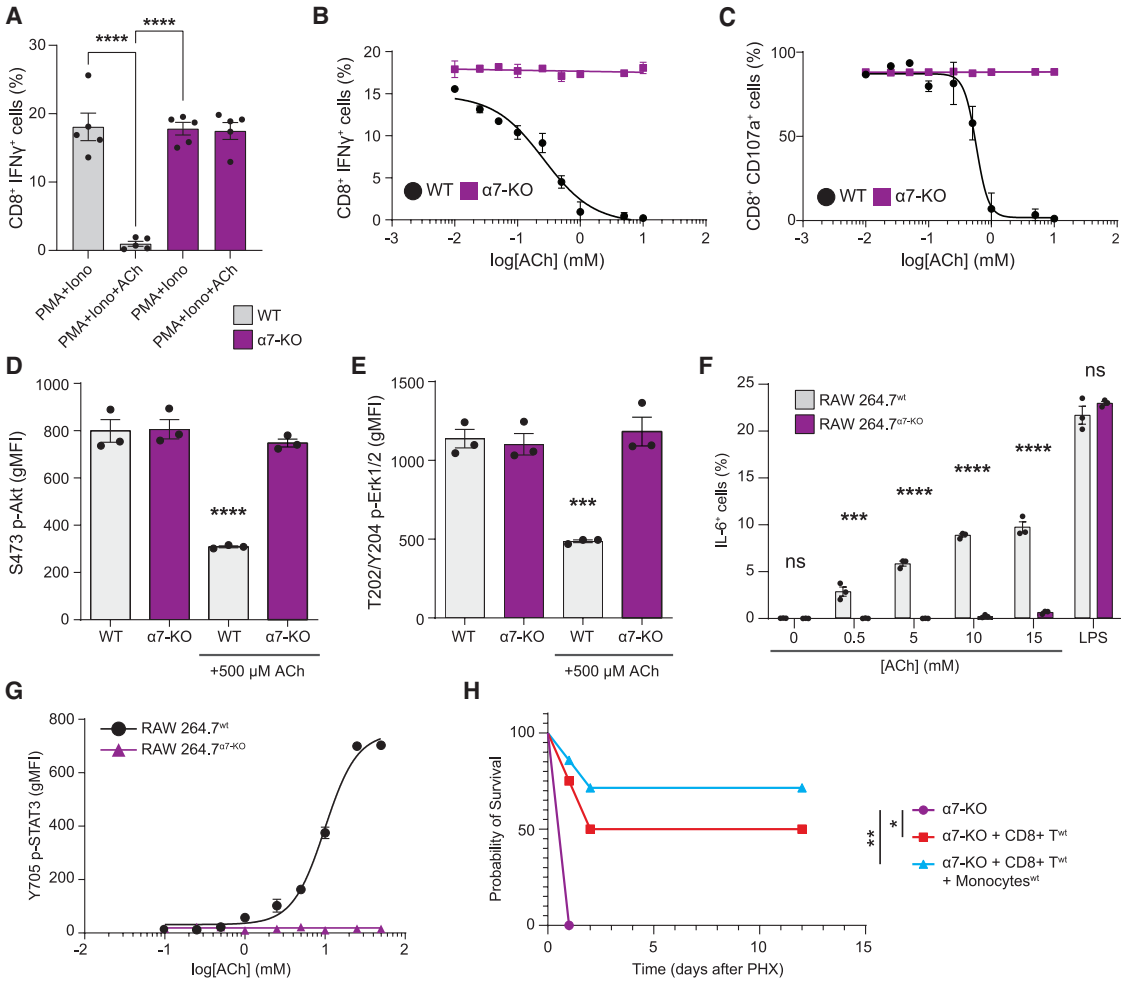

Figure 5. ChAT$^+$ B cells direct bi-axial regulation of LR through α7 AChR

(A) Quantitation of flow cytometric determination of percentages of IFNγ-producing hepatic CD8$^+$ T cells that were sorted from livers of naive WT or α7-KO mice (n = 5/group), treated *in vitro* with 500 μM ACh for 1 h, and activated by incubation with PMA/iono for 3 h at 37°C, 5% CO2. ****$p < 0.0001$ by one-way ANOVA.

(B and C) Log plots of flow cytometric determinations of percentages of IFNγ$^+$ (B) and CD107a$^+$ (C) CD8$^+$ T cells that were sorted from livers of naive WT and α7-KO mice (n = 3/group), treated *in vitro* with the indicated concentrations of ACh under serum-free conditions for 1 h, and stimulated for another 3 h with PMA/iono as in (A).

(D and E) Quantitation of flow cytometric analyses of p-AKT (S473) (D) and p-ERK1/2(T202/Y204) (E) in hepatic CD8$^+$ T cells that were sorted from naive WT or α7-KO mice and treated *in vitro* as in (A). ****$p < 0.0001$, ***$p = 0.0002$ by one-way ANOVA.

(F) Quantitation of flow cytometric determination of IL-6 production by RAW 264.7^{wt} and RAW 264.7$^{α7\text{-}ko}$ macrophages that were treated *in vitro* with the indicated concentrations of ACh for 4 h. LPS, a positive control in which cells were treated with LPS for 4 h at 37°C, 5% CO2 to induce activation. ****$p < 0.0001$ by two-way ANOVA.

(G) Log plot of flow cytometric determinations of STAT3 phosphorylation in RAW 264.7^{wt} and RAW 264.7$^{α7\text{-}ko}$ macrophages that were treated *in vitro* with the indicated ACh concentrations.

(H) Kaplan-Meier survival curves over 12 days following PHX of untreated α7-KO mice (n = 4), α7-KO mice reconstituted with WT CD8$^+$ T cells (n = 4), and α7-KO mice reconstituted with WT CD8$^+$ T cells plus WT BM-derived monocytes (n = 6). **$p = 0.0035$, *$p = 0.0133$ by log-rank (Mantel-Cox) test.

WT BM-derived monocytes and CD8$^+$ T cells from CD45.1$^+$ mice. Kupffer cells were depleted prior to adoptive transfer using clodronate liposomes, and then cells were adoptively transferred into α7-KO mice. These animals were then subjected to 70% PHX. Adoptive transfer of both cell populations simultaneously was even more effective at extending the survival of α7-KO mice post-PHX than was the transfer of WT CD8$^+$ T cells alone (Figure 5H). Thus, both signaling axes, namely ChAT$^+$ B cells to Kupffer cells and ChAT$^+$ B cells to CD8$^+$ T cells, serve crucial functions in LR.

Finally, we investigated the potential clinical relevance of our results using a human cell model. We isolated human peripheral blood mononuclear cells (PBMCs), which contain both T and B cells, from healthy donors and stimulated them under the same conditions as used for our mouse experiments shown in Figures S3M and S3L. Consistent with our murine data, ChAT expression was induced in human B cells stimulated with LPS or NE (Figures 6A and 6B). In addition, and again like our murine observations shown in Figures 5A–5D, stimulating human PBMCs with PMA/iono induced IFNγ production

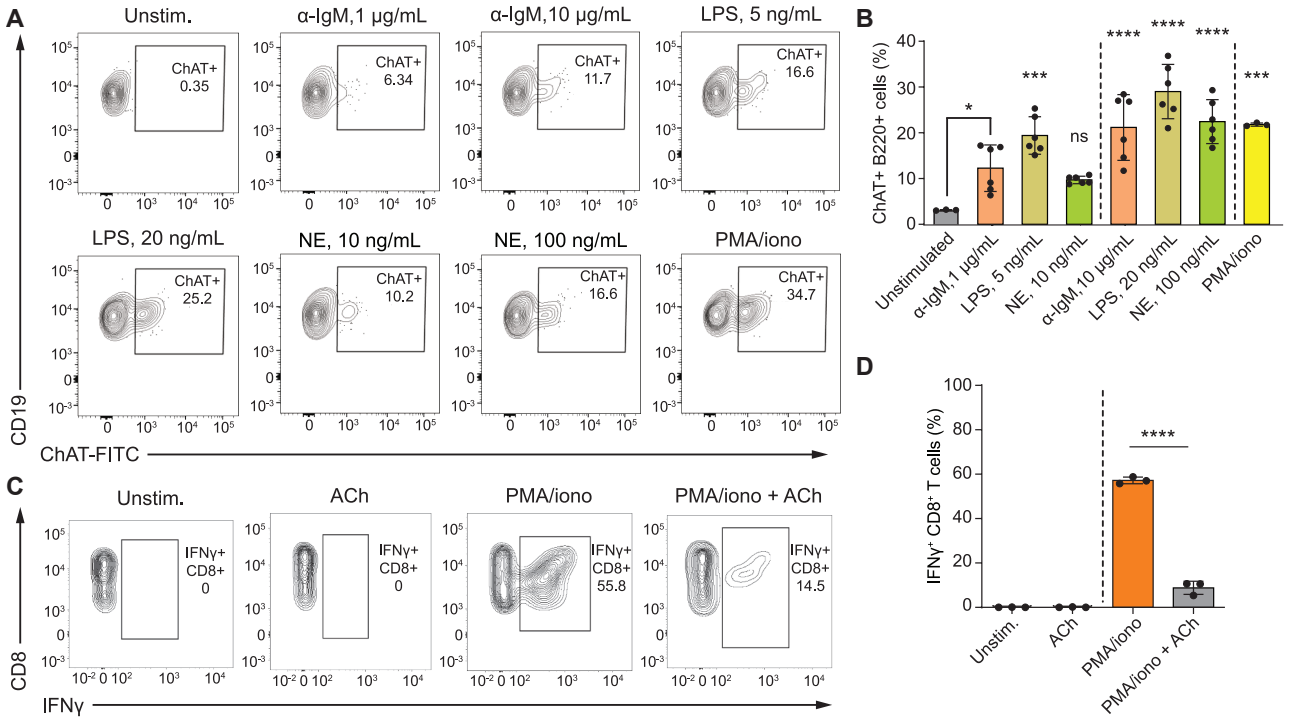

Figure 6. Human PBMCs include ChAT$^+$ B cells, and ACh suppresses IFNγ production by human CD8$^+$ T cells

(A) Representative flow cytometric plots of ChAT expression in B cells that were sorted from human PBMCs and left unstimulated or stimulated *in vitro* with the indicated concentrations of anti-IgM antibody, LPS, NE, or PMA/iono for 3 h at 37°C, 5% CO2.

(B) Quantitation of the data in (A) with $n = 6$ donors for all conditions, except PMA/iono and unstimulated ($n = 3$). ****$p < 0.0001$ by one-way ANOVA.

(C) Representative flow cytometric plots of IFNγ$^+$ CD8$^+$ T cells that were gated on whole human PBMCs and left unstimulated or treated *in vitro* for 3 h with 500 μM ACh alone, PMA/iono alone, or PMA/iono plus 500 μM ACh as in (A).

(D) Quantitation of the data in (C) with $n = 3$ donors for all conditions. ****$p < 0.0001$ by one-way ANOVA.

by CD8$^+$ T cells that was reversed in the presence of 500 μM ACh (Figures 6C and 6D). Thus, in both humans and mice, ACh-producing B cells exist, and ACh-mediated suppression of CD8$^+$ T cell-derived IFNγ production occurs, meaning that regulation of LR by cholinergic B cells may have broad clinical relevance.

DISCUSSION

Because LR is crucial for patient recovery after liver trauma or surgery,[57] a deeper understanding of this complex process and its major driving signals thus has the potential to identify new clinical targets and improve patient outcomes. Our study has demonstrated that the ACh produced by a hepatic subset of ChAT$^+$ B cells is a key factor in LR. These lymphocytes mediate bi-axial regulation that reduces IFNγ production by CD8$^+$ T cells but stimulates IL-6 synthesis by Kupffer cells, with both effects promoting hepatocyte survival and proliferation.

Organs generally receive innervation from both sympathetic and parasympathetic nerves, which influence organ function through neurotransmitter production. NE emanating from sympathetic nerves facilitates LR and hepatocyte proliferation,[3,58–61] and hepatic branch vagotomy disrupts LR and hepatocyte proliferation in rodent models after PHX.[1,2,62] The vagus nerve has also been cited as the source of ACh activating Kupffer cells during LR.[6–8,49] Although it is clear from these reports that ACh is critical for LR, numerous investigations (including those employing electron microscopy) in multiple species have revealed a conundrum. While sympathetic nerves do surround the hepatic artery, bile duct, and portal vein,[4,5] it is now generally accepted that parasympathetic innervation is undetectable in the liver parenchyma.[7,9,10] Our study has filled a gap in our knowledge of hepatic neurotransmitter function by conclusively identifying ChAT$^+$ B cells as the source of ACh crucial for LR.

Key hepatic cell types influenced by ChAT$^+$ B cells following PHX are Kupffer cells and CD8$^+$ T cells. With respect to the former, Kupffer cells are critical for producing the IL-6 necessary for hepatocyte proliferation during the early phase of LR.[33,36,63–65] Depletion of Kupffer cells in ChAT^{flox} mice increased mortality after PHX in a manner reversed by exogenous IL-6 treatment. This observation agrees with existing reports suggesting that an absence of Kupffer cells impairs LR, resulting in reduced IL-6, TNF, and hepatocyte growth factor (HGF).[63–65] Previous studies described the necessity of cholinergic neurotransmission for the activation of Kupffer cells and their cytokine production, but the source of ACh remained elusive.[6] Our study demonstrates that, in the absence of ChAT$^+$ B cells, Kupffer cells produce less IL-6 and have an anti-inflammatory phenotype characterized by *Il10*, *Hmox1*, and *Ripk3* expression. An IL-10/HMOX1 axis inhibits cytokine production by macrophages,[38] and elevated RIPK3 is

associated with the progression of liver inflammation and liver cancer.[66] Thus, ACh from ChAT$^+$ B cells may not only promote IL-6 production but may also suppress an anti-inflammatory phenotype of Kupffer cells that would preclude LR.

With respect to CD8$^+$ T cells, it is their contribution to the inflammatory milieu that must be tightly regulated for hepatocytes to proliferate normally during LR. Excessive IFNγ triggers hepatocyte apoptosis and disrupts the cell cycle.[41,42,67,68] Accordingly, suppression of IFNγ signaling has been proposed as a strategy to reduce allograft rejection following liver transplantation and for the treatment of non-alcoholic steatohepatitis (NASH).[41,69] In a healthy liver subjected to PHX, a decrease in IFNγ production occurs during the 24 h of LR that presumably allows hepatocytes to proliferate.[40] We found that, in the absence of ChAT$^+$ B cells, there were sharp increases in the numbers of both IFNγ-producing CD8$^+$ T cells and IFNγ-responding hepatocytes in regenerating mouse liver. Depletion of these CD8$^+$ T cells restored the viability of ChAT$^{flox;Mb1\text{-}Cre}$ mice post-PHX. Thus, ChAT$^+$ B cells activated during the early hours post-PHX may control the liver's inflammatory milieu (particularly IFNγ levels) and protect against T cell-mediated hepatotoxicity.

As noted above, ACh-AChR binding has numerous modulatory effects on immune cell functions.[43–47,70] We confirmed α7 AChR expression in Kupffer cells and CD8$^+$ T cells and validated that loss of this receptor leads to a post-PHX phenotype parallel to that of ChAT$^{flox;Mb1\text{-}Cre}$ mice. In line with reports that AKT and MAPK/ERK signaling can induce IFNγ production,[51,71] we showed that ACh stimulation of CD8$^+$ T cells diminishes IFNγ production by reducing AKT and ERK phosphorylation. Similarly, ACh stimulation of RAW 264.7^{wt} cells induced IL-6 production and STAT3 phosphorylation in an α7 nAChR-dependent manner. The absence of these effects in RAW 264.7$^{\alpha7\text{-}ko}$ cells highlights the critical role of ACh/α7 nAChR signaling in regulating these pathways, which may contribute to the altered Kupffer cell function seen in ChAT$^{flox;Mb1\text{-}Cre}$ mice.

In conclusion, our study has revealed that ChAT$^+$ B cells play a pivotal bi-axial role during LR. Our study has thus contributed valuable insights with translation potential to human studies and may guide the development of improved therapeutics to combat the increasingly high mortality rates of liver-associated diseases. Moreover, because ChAT$^+$ B cells do exist in other tissues[72] and may have systemic effects beyond the liver, the exploration of their properties may provide broader insights into the functions of lymphocyte-derived neurotransmitters in systemic immune regulation and organ regeneration.

Limitations of the study

Our study does leave unresolved certain issues that will have to be addressed in future studies. (1) Our focus on the α7 AChR stemmed from our analyses of published spatial transcriptomics data,[40] and these data indicated that only *Chrna7*$^+$ spots co-localized between B cells, CD8$^+$ T cells, and Kupffer cells post-PHX. However, as illustrated in Figure S6B, these analyses also revealed extensive spatiotemporal regulation of other AChRs during LR, a finding that should spark the characterization of additional roles for ChAT$^+$ B cells and/or the identification of alternative recipients of their ACh. Our future work will include the examination of these receptors' functions during LR. (2) Our experiments indicated that both ChAT$^+$ B cell-Kupffer cell and ChAT$^+$ B cell-CD8$^+$ T cell interactions are crucial for LR. Future studies utilizing cell type-specific conditional KO models will be necessary to determine the dominant pathway driven by ChAT$^+$ B cells and its mechanistic underpinnings. (3) Previous studies have suggested that IgA$^+$ B cells promote liver fibrosis through CXCR4-CXCL12 interaction, implying that CXCR4 expression by B cells may impede LR.[73,74] However, we found that GFP$^+$ B cells do not express IgA, and our bulk RNA sequencing results revealed significantly diminished *Cxcr4* expression by GFP$^+$ B cells from ChAT-GFP mice. It may be that the pro-fibrotic axis is downregulated in ChAT$^+$ B cells in favor of pro-regenerative features, a hypothesis requiring additional investigation. (4) Given that NE can induce ChAT expression in WT B cells *in vitro*, we intend to study the effects of NE on ChAT$^+$ B cells *in vivo* in detail. (5) With respect to human data, it was challenging to obtain sufficient appropriate patient liver tissue samples after PHX with which to assess the presence of ChAT$^+$ B cells in the human liver. As an alternative, we will consider the use of human liver organoids as a means of investigating the impact of ChAT$^+$ B cells on human hepatocytes.

RESOURCE AVAILABILITY

Lead contact

Further information and requests for resources and reagents should be directed to and will be fulfilled by the lead contact, Dr. T.W. Mak (email: tak.mak@uhn.ca).

Materials availability

This study did not generate new, unique reagents. All transgenic mice used in this study are available from The Jackson Laboratory or in Dr. Tak Mak's laboratory.

Data and materials availability

Bulk and scRNA-seq data generated in this study have been deposited at GEO and are publicly available as of the date of publication. Accession numbers are listed in the key resources table. Previously published spatial and scRNA-seq data of the regenerating liver from Xu et al., leveraged in this study, are publicly available. The link used to access the data for this study is provided in the key resources table. All original code has been deposited at Zenodo and is publicly available as of the date of publication. DOIs are listed in the key resources table. All original data of this study are available and can be provided by the lead contact upon request.

Any additional information required to reanalyze the data reported in this paper is available from the lead contact upon request.

ACKNOWLEDGMENTS

This work was supported by grants to T.W.M. from the Canadian Institutes for Health Research, Ottawa, Canada and from the Centre for Oncology and Immunology under the Health@InnoHK Initiative funded by the Innovation and Technology Commission, The Government of Hong Kong SAR, China. N.F.M. was supported by an Irvington Fellowship from the Cancer Research Institute (USA). We thank Maureen Cox, Julie Leca, Robert Nechanitzky, Duygu Nechanitzky, Shawn Kubli, Claus Kordes, and Klaus Pfeffer and Philipp A. Lang for scientific advice and helpful discussions; Wenjing Zhou, Dat Nguyen, Nisha Ramamurthy, and Annick You-Ten for technical help in the laboratory; Irene Ng for administrative assistance; and Xin Zhang for intravenous (i.v.) injections. The authors are also grateful to Andrew Elia and Rhoda Law of the Princess Margaret HistoCore (UHN) for histological imaging; all staff of the Animal Resource Centre at Princess Margaret Hospital for animal care; and Arian Khandani and Aleks Spurmanis of the PMFlow Cytometry Core Facility (UHN) for isolation of B cells, CD8+ T cells, and Kupffer cell populations and for establishing the marker panel for sample acquisition.

AUTHOR CONTRIBUTIONS

N.F.M. and T.W.M. conceptualized the project. N.F.M. designed and conducted experiments. N.F.M., L.D.H., and M.S.P. wrote the initial draft of the manuscript. N.F.M., L.K.S., R.N., E.F., S.M.J., F.K.T., and I.C. helped with and conducted experiments. L.D.H. and P.L. analyzed bioinformatics data. R.B. conducted mass spectrometry experiments. P.K., B.A.D., T.R., and W-Y.L. performed IVM. M.S.P. and S.H. designed guide RNA and generated RAW 264.7$^{\alpha7\text{-ko}}$ cells. J.H., M.B., and R.M. helped to genotype all mouse strains used in this study and were responsible for breeding genetically modified strains. T.K. assisted with bulk and scRNA-seq experiments. M.E.S. provided scientific editing advice and edited the manuscript. S.L., C.Z., and J.F. contributed scientific insights to the project. A.C.W. and J.S. assisted in obtaining the required reagents and materials. T.B., A.C.W., and T.W.M. acquired funding.

DECLARATION OF INTERESTS

T.W.M. owns equity in Treadwell Therapeutics and is a consultant for AstraZeneca. A patent application is being submitted.

STAR★METHODS

Detailed methods are provided in the online version of this paper and include the following:

- KEY RESOURCES TABLE
- EXPERIMENTAL MODEL AND STUDY PARTICIPANT DETAILS
  - Mouse strains
- METHOD DETAILS
  - Partial hepatectomy and splenectomy of mice
  - Serum analyses
  - Cyclin D1 determinations by IHC staining and quantitative real time-PCR
  - H&E staining
  - Isolation of liver lymphocytes
  - Generation of RAW 264.7α7-KO cells
  - Mass spectrometry of liver tissue
  - Parallel Reaction Monitoring (PRM)
  - Flow cytometric cell sorting and cytokine detection
  - Cytokine detection following in vitro ACh treatment
  - Phospho-specific flow cytometry
  - Adoptive transfer
  - *In vivo* depletion of CD8$^+$, NK1.1+ and Kupffer cells and IL-6 injection
  - Norepinephrine and LPS in vitro stimulations of human PBMCs and mouse B cells
  - mRNA expression of nicotinic and muscarinic ACh receptor genes
  - Flow cytometric determination of surface expression of nAChR and mAChR proteins
  - B cell isolation, mRNA library construction, and bulk RNA sequencing
  - Immune repertoire reconstruction from bulk RNA sequencing
  - Alignment, processing, and analysis of ChAT+ B cell bulk RNA sequencing data
  - Pathway enrichment analysis
  - Single-cell RNA sequencing (scRNAseq) library preparation, sequencing, and alignment
  - Quality control and normalization of scRNAseq libraries
  - Integration and cell type annotation of scRNAseq libraries
  - Hepatic immune cell sub-clustering
  - Kupffer cell pseudotime trajectory analysis
  - Single-cell gene expression density visualizations
  - Analysis of scRNAseq and spatial transcriptomics of liver regeneration
- QUALIFICATION AND STATISTICAL ANALYSIS

SUPPLEMENTAL INFORMATION

Supplemental information can be found online at https://doi.org/10.1016/j.immuni.2025.04.002.

Received: July 9, 2024
Revised: December 20, 2024
Accepted: April 2, 2025
Published: April 25, 2025

REFERENCES

1. Kato, H., and Shimazu, T. (1983). Effect of autonomic denervation on DNA synthesis during liver regeneration after partial hepatectomy. Eur. J. Biochem. *134*, 473–478. https://doi.org/10.1111/j.1432-1033.1983.tb07591.x.
2. Tanaka, K., Ohkawa, S., Nishino, T., Niijima, A., and Inoue, S. (1987). Role of the hepatic branch of the vagus nerve in liver regeneration in rats. Am. J. Physiol. *253*, G439–G444. https://doi.org/10.1152/ajpgi.1987.253.4.G439.
3. Ohtake, Y., Kobayashi, T., Maruko, A., Oh-Ishi, N., Yamamoto, F., Katoh, S., and Ohkubo, Y. (2010). Norepinephrine modulates the zonally different hepatocyte proliferation through the regulation of transglutaminase activity. Am. J. Physiol. Gastrointest. Liver Physiol. *299*, G106–G114. https://doi.org/10.1152/ajpgi.00365.2009.
4. Nobin, A., Baumgarten, H.G., Falck, B., Ingemansson, S., Moghimzadeh, E., and Rosengren, E. (1978). Organization of the sympathetic innervation in liver tissue from monkey and man. Cell Tissue Res. *195*, 371–380. https://doi.org/10.1007/BF00233883.
5. Tsuneki, K., and Ichihara, K. (1981). Electron microscope study of vertebrate liver innervation. Arch. Histol. Jpn. *44*, 1–13. https://doi.org/10.1679/aohc1950.44.1.
6. Izumi, T., Imai, J., Yamamoto, J., Kawana, Y., Endo, A., Sugawara, H., Kohata, M., Asai, Y., Takahashi, K., Kodama, S., et al. (2018). Vagus-macrophage-hepatocyte link promotes post-injury liver regeneration and whole-body survival through hepatic FoxM1 activation. Nat. Commun. *9*, 5300. https://doi.org/10.1038/s41467-018-07747-0.
7. Ikeda, O., Ozaki, M., Murata, S., Matsuo, R., Nakano, Y., Watanabe, M., Hisakura, K., Myronovych, A., Kawasaki, T., Kohno, K., and Ohkohchi, N. (2009). Autonomic regulation of liver regeneration after partial hepatectomy in mice. J. Surg. Res. *152*, 218–223. https://doi.org/10.1016/j.jss.2008.02.059.
8. Kimura, K., Tanida, M., Nagata, N., Inaba, Y., Watanabe, H., Nagashimada, M., Ota, T., Asahara, S., Kido, Y., Matsumoto, M., et al. (2016). Central Insulin Action Activates Kupffer Cells by Suppressing Hepatic Vagal Activation via the Nicotinic Alpha 7 Acetylcholine Receptor. Cell Rep. *14*, 2362–2374. https://doi.org/10.1016/j.celrep.2016.02.032.
9. Fukuda, Y., Imoto, M., Koyama, Y., Miyazawa, Y., and Hayakawa, T. (1996). Demonstration of noradrenaline-immunoreactive nerve fibres in the liver. J. Int. Med. Res. *24*, 466–472. https://doi.org/10.1177/030006059602400603.
10. Adori, C., Daraio, T., Kuiper, R., Barde, S., Horvathova, L., Yoshitake, T., Ihnatko, R., Valladolid-Acebes, I., Vercruysse, P., Wellendorf, A.M., et al. (2021). Disorganization and degeneration of liver sympathetic innervations in nonalcoholic fatty liver disease revealed by 3D imaging. Sci. Adv. *7*, eabg5733. https://doi.org/10.1126/sciadv.abg5733.
11. Jensen, K.J., Alpini, G., and Glaser, S. (2013). Hepatic nervous system and neurobiology of the liver. Compr. Physiol. *3*, 655–665. https://doi.org/10.1002/cphy.c120018.
12. Berthoud, H.R., Kressel, M., and Neuhuber, W.L. (1992). An anterograde tracing study of the vagal innervation of rat liver, portal vein and biliary system. Anat. Embryol. (Berl.) *186*, 431–442. https://doi.org/10.1007/BF00185458.

13. Akiyoshi, H., Gonda, T., and Terada, T. (1998). A comparative histochemical and immunohistochemical study of aminergic, cholinergic and peptidergic innervation in rat, hamster, guinea pig, dog and human livers. Liver *18*, 352–359. https://doi.org/10.1111/j.1600-0676.1998.tb00817.x.

14. Liu, K., Yang, L., Wang, G., Liu, J., Zhao, X., Wang, Y., Li, J., and Yang, J. (2021). Metabolic stress drives sympathetic neuropathy within the liver. Cell Metab. *33*, 666–675.e4. https://doi.org/10.1016/j.cmet.2021.01.012.

15. Cox, M.A., Duncan, G.S., Lin, G.H.Y., Steinberg, B.E., Yu, L.X., Brenner, D., Buckler, L.N., Elia, A.J., Wakeham, A.C., Nieman, B., et al. (2019). Choline acetyltransferase-expressing T cells are required to control chronic viral infection. Science *363*, 639–644. https://doi.org/10.1126/science.aau9072.

16. Zheng, C., Snow, B.E., Elia, A.J., Nechanitzky, R., Dominguez-Brauer, C., Liu, S., Tong, Y., Cox, M.A., Focaccia, E., Wakeham, A.C., et al. (2023). Tumor-specific cholinergic CD4+ T lymphocytes guide immunosurveillance of hepatocellular carcinoma. Nat. Cancer *4*, 1437–1454. https://doi.org/10.1038/s43018-023-00624-w.

17. Nechanitzky, R., Nechanitzky, D., Ramachandran, P., Duncan, G.S., Zheng, C., Göbl, C., Gill, K.T., Haight, J., Wakeham, A.C., Snow, B.E., et al. (2023). Cholinergic control of Th17 cell pathogenicity in experimental autoimmune encephalomyelitis. Cell Death Differ. *30*, 407–416. https://doi.org/10.1038/s41418-022-01092-y.

18. Reardon, C., Duncan, G.S., Brüstle, A., Brenner, D., Tusche, M.W., Olofsson, P.S., Rosas-Ballina, M., Tracey, K.J., and Mak, T.W. (2013). Lymphocyte-derived ACh regulates local innate but not adaptive immunity. Proc. Natl. Acad. Sci. USA *110*, 1410–1415. https://doi.org/10.1073/pnas.1221655110.

19. Takeishi, T., Hirano, K., Kobayashi, T., Hasegawa, G., Hatakeyama, K., and Naito, M. (1999). The role of Kupffer cells in liver regeneration. Arch. Histol. Cytol. *62*, 413–422. https://doi.org/10.1679/aohc.62.413.

20. Behnke, K., Zhuang, Y., Xu, H.C., Sundaram, B., Reich, M., Shinde, P.V., Huang, J., Modares, N.F., Tumanov, A.V., Polz, R., et al. (2018). B Cell-Mediated Maintenance of Cluster of Differentiation 169-Positive Cells Is Critical for Liver Regeneration. Hepatology *68*, 2348–2361. https://doi.org/10.1002/hep.30088.

21. Tumanov, A.V., Koroleva, E.P., Christiansen, P.A., Khan, M.A., Ruddy, M. J., Burnette, B., Papa, S., Franzoso, G., Nedospasov, S.A., Fu, Y.X., et al. (2009). T cell-derived lymphotoxin regulates liver regeneration. Gastroenterology *136*, 694–704.e4. https://doi.org/10.1053/j.gastro.2008.09.015.

22. Chou, C.H., Ho, C.M., Lai, S.L., Chen, C.N., Wu, Y.M., Shun, C.T., Wen, W. F., and Lai, H.S. (2019). B-Cell Activating Factor Enhances Hepatocyte-Driven Angiogenesis via B-Cell CLL/Lymphoma 10/Nuclear Factor-KappaB Signaling during Liver Regeneration. Int. J. Mol. Sci. *20*, 5022. https://doi.org/10.3390/ijms20205022.

23. Song, L., Cohen, D., Ouyang, Z., Cao, Y., Hu, X., and Liu, X.S. (2021). TRUST4: immune repertoire reconstruction from bulk and single-cell RNA-seq data. Nat. Methods *18*, 627–630. https://doi.org/10.1038/s41592-021-01142-2.

24. Baumgarth, N. (2016). B-1 Cell Heterogeneity and the Regulation of Natural and Antigen-Induced IgM Production. Front. Immunol. *7*, 324. https://doi.org/10.3389/fimmu.2016.00324.

25. Rosas-Ballina, M., Olofsson, P.S., Ochani, M., Valdés-Ferrer, S.I., Levine, Y.A., Reardon, C., Tusche, M.W., Pavlov, V.A., Andersson, U., Chavan, S., et al. (2011). Acetylcholine-synthesizing T cells relay neural signals in a vagus nerve circuit. Science *334*, 98–101. https://doi.org/10.1126/science.1209985.

26. Takahashi, M., Ogasawara, K., Takeda, K., Hashimoto, W., Sakihara, H., Kumagai, K., Anzai, R., Satoh, M., and Seki, S. (1996). LPS induces NK1.1+ alpha beta T cells with potent cytotoxicity in the liver of mice via production of IL-12 from Kupffer cells. J. Immunol. *156*, 2436–2442.

27. Yagi, S., Hirata, M., Miyachi, Y., and Uemoto, S. (2020). Liver Regeneration after Hepatectomy and Partial Liver Transplantation. Int. J. Mol. Sci. *21*, 8414. https://doi.org/10.3390/ijms21218414.

28. Wilkinson, P.D., and Duncan, A.W. (2021). Differential Roles for Diploid and Polyploid Hepatocytes in Acute and Chronic Liver Injury. Semin. Liver Dis. *41*, 42–49. https://doi.org/10.1055/s-0040-1719175.

29. MacParland, S.A., Liu, J.C., Ma, X.Z., Innes, B.T., Bartczak, A.M., Gage, B. K., Manuel, J., Khuu, N., Echeverri, J., Linares, I., et al. (2018). Single cell RNA sequencing of human liver reveals distinct intrahepatic macrophage populations. Nat. Commun. *9*, 4383. https://doi.org/10.1038/s41467-018-06318-7.

30. Wilkinson, P.D., Delgado, E.R., Alencastro, F., Leek, M.P., Roy, N., Weirich, M.P., Stahl, E.C., Otero, P.A., Chen, M.I., Brown, W.K., et al. (2019). The Polyploid State Restricts Hepatocyte Proliferation and Liver Regeneration in Mice. Hepatology *69*, 1242–1258. https://doi.org/10.1002/hep.30286.

31. Streetz, K.L., Luedde, T., Manns, M.P., and Trautwein, C. (2000). Interleukin 6 and liver regeneration. Gut *47*, 309–312. https://doi.org/10.1136/gut.47.2.309.

32. Michalopoulos, G.K. (2010). Liver regeneration after partial hepatectomy: critical analysis of mechanistic dilemmas. Am. J. Pathol. *176*, 2–13. https://doi.org/10.2353/ajpath.2010.090675.

33. Fazel Modares, N., Polz, R., Haghighi, F., Lamertz, L., Behnke, K., Zhuang, Y., Kordes, C., Häussinger, D., Sorg, U.R., Pfeffer, K., et al. (2019). IL-6 Trans-signaling Controls Liver Regeneration After Partial Hepatectomy. Hepatology *70*, 2075–2091. https://doi.org/10.1002/hep.30774.

34. Scheller, J., Garbers, C., and Rose-John, S. (2014). Interleukin-6: from basic biology to selective blockade of pro-inflammatory activities. Semin. Immunol. *26*, 2–12. https://doi.org/10.1016/j.smim.2013.11.002.

35. Wang, L., Walia, B., Evans, J., Gewirtz, A.T., Merlin, D., and Sitaraman, S. V. (2003). IL-6 induces NF-kappa B activation in the intestinal epithelia. J. Immunol. *171*, 3194–3201. https://doi.org/10.4049/jimmunol.171.6.3194.

36. Taub, R. (2004). Liver regeneration: from myth to mechanism. Nat. Rev. Mol. Cell Biol. *5*, 836–847. https://doi.org/10.1038/nrm1489.

37. Knolle, P., Schlaak, J., Uhrig, A., Kempf, P., Meyer zum Büschenfelde, K. H., and Gerken, G. (1995). Human Kupffer cells secrete IL-10 in response to lipopolysaccharide (LPS) challenge. J. Hepatol. *22*, 226–229. https://doi.org/10.1016/0168-8278(95)80433-1.

38. Kuwata, H., Watanabe, Y., Miyoshi, H., Yamamoto, M., Kaisho, T., Takeda, K., and Akira, S. (2003). IL-10-inducible Bcl-3 negatively regulates LPS-induced TNF-alpha production in macrophages. Blood *102*, 4123–4129. https://doi.org/10.1182/blood-2003-04-1228.

39. Sturm, E., Havinga, R., Baller, J.F.W., Wolters, H., van Rooijen, N., Kamps, J.A.A.M., Verkade, H.J., Karpen, S.J., and Kuipers, F. (2005). Kupffer cell depletion with liposomal clodronate prevents suppression of Ntcp expression in endotoxin-treated rats. J. Hepatol. *42*, 102–109. https://doi.org/10.1016/j.jhep.2004.09.019.

40. Xu, J., Guo, P., Hao, S., Shangguan, S., Shi, Q., Volpe, G., Huang, K., Zuo, J., An, J., Yuan, Y., et al. (2024). A spatiotemporal atlas of mouse liver homeostasis and regeneration. Nat. Genet. *56*, 953–969. https://doi.org/10.1038/s41588-024-01709-7.

41. Horras, C.J., Lamb, C.L., and Mitchell, K.A. (2011). Regulation of hepatocyte fate by interferon-γ. Cytokine Growth Factor Rev. *22*, 35–43. https://doi.org/10.1016/j.cytogfr.2011.01.001.

42. Dudek, M., Pfister, D., Donakonda, S., Filpe, P., Schneider, A., Laschinger, M., Hartmann, D., Hüser, N., Meiser, P., Bayerl, F., et al. (2021). Auto-aggressive CXCR6+ CD8 T cells cause liver immune pathology in NASH. Nature *592*, 444–449. https://doi.org/10.1038/s41586-021-03233-8.

43. Tracey, K.J., Beutler, B., Lowry, S.F., Merryweather, J., Wolpe, S., Milsark, I.W., Hariri, R.J., Fahey, T.J., 3rd, Zentella, A., and Albert, J.D. (1986). Shock and tissue injury induced by recombinant human cachectin. Science *234*, 470–474. https://doi.org/10.1126/science.3764421.

44. Tracey, K.J. (2002). The inflammatory reflex. Nature *420*, 853–859. https://doi.org/10.1038/nature01321.

45. Tracey, K.J., Fong, Y., Hesse, D.G., Manogue, K.R., Lee, A.T., Kuo, G.C., Lowry, S.F., and Cerami, A. (1987). Anti-cachectin/TNF monoclonal

antibodies prevent septic shock during lethal bacteraemia. Nature *330*, 662–664. https://doi.org/10.1038/330662a0.

46. Jones, C.K., Byun, N., and Bubser, M. (2012). Muscarinic and nicotinic acetylcholine receptor agonists and allosteric modulators for the treatment of schizophrenia. Neuropsychopharmacology *37*, 16–42. https://doi.org/10.1038/npp.2011.199.

47. Razani-Boroujerdi, S., Boyd, R.T., Dávila-García, M.I., Nandi, J.S., Mishra, N.C., Singh, S.P., Pena-Philippides, J.C., Langley, R., and Sopori, M.L. (2007). T cells express alpha7-nicotinic acetylcholine receptor subunits that require a functional TCR and leukocyte-specific protein tyrosine kinase for nicotine-induced Ca2+ response. J. Immunol. *179*, 2889–2898. https://doi.org/10.4049/jimmunol.179.5.2889.

48. Cable, D.M., Murray, E., Zou, L.S., Goeva, A., Macosko, E.Z., Chen, F., and Irizarry, R.A. (2022). Robust decomposition of cell type mixtures in spatial transcriptomics. Nat. Biotechnol. *40*, 517–526. https://doi.org/10.1038/s41587-021-00830-w.

49. Soukup, O., Winder, M., Killi, U.K., Wsol, V., Jun, D., Kuca, K., and Tobin, G. (2017). Acetylcholinesterase Inhibitors and Drugs Acting on Muscarinic Receptors- Potential Crosstalk of Cholinergic Mechanisms During Pharmacological Treatment. Curr. Neuropharmacol. *15*, 637–653. https://doi.org/10.2174/1570159X14666160607212615.

50. Rodrigues, L.S., Barreto, A.S., Bomfim, L.G.S., Gomes, M.C., Ferreira, N. L.C., da Cruz, G.S., Magalhães, L.S., de Jesus, A.R., Palatnik-de-Sousa, C.B., Corrêa, C.B., and de Almeida, R.P. (2021). Multifunctional, TNF-alpha and IFN-gamma-Secreting CD4 and CD8 T Cells and CD8High T Cells Are Associated With the Cure of Human Visceral Leishmaniasis. Front. Immunol. *12*, 773983. https://doi.org/10.3389/fimmu.2021.773983.

51. Santinon, F., Ezzahra, B.F., Bachais, M., Sarabia Pacis, A., and Rudd, C.E. (2022). Direct AKT activation in tumor-infiltrating lymphocytes markedly increases interferon-γ (IFN-γ) for the regression of tumors resistant to PD-1 checkpoint blockade. Sci. Rep. *12*, 18509. https://doi.org/10.1038/s41598-022-23016-z.

52. Cressman, D.E., Greenbaum, L.E., DeAngelis, R.A., Ciliberto, G., Furth, E. E., Poli, V., and Taub, R. (1996). Liver failure and defective hepatocyte regeneration in interleukin-6-deficient mice. Science *274*, 1379–1383. https://doi.org/10.1126/science.274.5291.1379.

53. Trautwein, C., Rakemann, T., Niehof, M., Rose-John, S., and Manns, M.P. (1996). Acute-phase response factor, increased binding, and target gene transcription during liver regeneration. Gastroenterology *110*, 1854–1862. https://doi.org/10.1053/gast.1996.v110.pm8964411.

54. Schmidt-Arras, D., and Rose-John, S. (2016). IL-6 pathway in the liver: From physiopathology to therapy. J. Hepatol. *64*, 1403–1415. https://doi.org/10.1016/j.jhep.2016.02.004.

55. Scott, C.L., Zheng, F., De Baetselier, P., Martens, L., Saeys, Y., De Prijck, S., Lippens, S., Abels, C., Schoonooghe, S., Raes, G., et al. (2016). Bone marrow-derived monocytes give rise to self-renewing and fully differentiated Kupffer cells. Nat. Commun. *7*, 10321. https://doi.org/10.1038/ncomms10321.

56. Li, W., Yang, Y., Yang, L., Chang, N., and Li, L. (2023). Monocyte-derived Kupffer cells dominate in the Kupffer cell pool during liver injury. Cell Rep. *42*, 113164. https://doi.org/10.1016/j.celrep.2023.113164.

57. Michalopoulos, G.K. (2007). Liver regeneration. J. Cell. Physiol. *213*, 286–300. https://doi.org/10.1002/jcp.21172.

58. Wang, W., Hu, C.K., Zeng, A., Alegre, D., Hu, D., Gotting, K., Ortega Granillo, A., Wang, Y., Robb, S., Schnittker, R., et al. (2020). Changes in regeneration-responsive enhancers shape regenerative capacities in vertebrates. Science *369*, eaaz3090. https://doi.org/10.1126/science.aaz3090.

59. Poss, K.D. (2010). Advances in understanding tissue regenerative capacity and mechanisms in animals. Nat. Rev. Genet. *11*, 710–722. https://doi.org/10.1038/nrg2879.

60. Matsuda, H., Koyama, H., Sato, H., Sawada, J., Itakura, A., Tanaka, A., Matsumoto, M., Konno, K., Ushio, H., and Matsuda, K. (1998). Role of nerve growth factor in cutaneous wound healing: accelerating effects in normal and healing-impaired diabetic mice. J. Exp. Med. *187*, 297–306. https://doi.org/10.1084/jem.187.3.297.

61. Gupta, D., Kaushik, D., and Mohan, V. (2022). Role of neurotransmitters in the regulation of cutaneous wound healing. Exp. Brain Res. *240*, 1649–1659. https://doi.org/10.1007/s00221-022-06372-0.

62. Ohtake, M., Sakaguchi, T., Yoshida, K., and Muto, T. (1993). Hepatic branch vagotomy can suppress liver regeneration in partially hepatectomized rats. HPB Surg. *6*, 277–286. https://doi.org/10.1155/1993/59691.

63. Meijer, C., Wiezer, M.J., Diehl, A.M., Schouten, H.J., Schouten, H.J., Meijer, S., van Rooijen, N., van Lambalgen, A.A., Dijkstra, C.D., and van Leeuwen, P.A. (2000). Kupffer cell depletion by CI2MDP-liposomes alters hepatic cytokine expression and delays liver regeneration after partial hepatectomy. Liver *20*, 66–77. https://doi.org/10.1034/j.1600-0676.2000.020001066.x.

64. Abshagen, K., Eipel, C., Kalff, J.C., Menger, M.D., and Vollmar, B. (2007). Loss of NF-kappaB activation in Kupffer cell-depleted mice impairs liver regeneration after partial hepatectomy. Am. J. Physiol. Gastrointest. Liver Physiol. *292*, G1570–G1577. https://doi.org/10.1152/ajpgi.00399.2006.

65. Boulton, R.A., Alison, M.R., Golding, M., Selden, C., and Hodgson, H.J. (1998). Augmentation of the early phase of liver regeneration after 70% partial hepatectomy in rats following selective Kupffer cell depletion. J. Hepatol. *29*, 271–280. https://doi.org/10.1016/s0168-8278(98)80013-5.

66. Vucur, M., Ghallab, A., Schneider, A.T., Adili, A., Cheng, M., Castoldi, M., Singer, M.T., Büttner, V., Keysberg, L.S., Küsgens, L., et al. (2023). Sublethal necroptosis signaling promotes inflammation and liver cancer. Immunity *56*, 1578–1595.e8. https://doi.org/10.1016/j.immuni.2023.05.017.

67. Roth, E., and Pircher, H. (2004). IFN-gamma promotes Fas ligand- and perforin-mediated liver cell destruction by cytotoxic CD8 T cells. J. Immunol. *172*, 1588–1594. https://doi.org/10.4049/jimmunol.172.3.1588.

68. Koda, Y., Teratani, T., Chu, P.S., Hagihara, Y., Mikami, Y., Harada, Y., Tsujikawa, H., Miyamoto, K., Suzuki, T., Taniki, N., et al. (2021). CD8+ tissue-resident memory T cells promote liver fibrosis resolution by inducing apoptosis of hepatic stellate cells. Nat. Commun. *12*, 4474. https://doi.org/10.1038/s41467-021-24734-0.

69. Okita, R., Shimizu, K., Nojima, Y., Saisho, S., and Nakata, M. (2021). Tofacitinib overcomes an IFNgamma-induced decrease in NK cell-mediated cytotoxicity via the regulation of immune-related molecules in LC-2/ad. Thorac. Cancer *12*, 775–782. https://doi.org/10.1111/1759-7714.13847.

70. Wasén, C., Turkkila, M., Bossios, A., Erlandsson, M., Andersson, K.M., Ekerljung, L., Malmhäll, C., Brisslert, M., Töyrä Silfverswärd, S., Lundbäck, B., et al. (2017). Smoking activates cytotoxic CD8+ T cells and causes survivin release in rheumatoid arthritis. J. Autoimmun. *78*, 101–110. https://doi.org/10.1016/j.jaut.2016.12.009.

71. Jacques-Silva, M.C., Rodnight, R., Lenz, G., Liao, Z., Kong, Q., Tran, M., Kang, Y., Gonzalez, F.A., Weisman, G.A., and Neary, J.T. (2004). P2X7 receptors stimulate AKT phosphorylation in astrocytes. Br. J. Pharmacol. *141*, 1106–1117. https://doi.org/10.1038/sj.bjp.0705685.

72. Baumgarth, N., Prieto, A.C., Luo, Z., and Kulaga, H. (2024). B cells modulate lung antiviral inflammatory responses via the neurotransmitter acetylcholine. Res Sq, rs.3.rs-4421566. https://doi.org/10.21203/rs.3.rs-4421566/v1.

73. Zhang, L., Zhao, C., Dai, W., Tong, H., Yang, W., Huang, Z., Tang, C., and Gao, J. (2023). Disruption of cholangiocyte-B cell crosstalk by blocking the CXCL12-CXCR4 axis alleviates liver fibrosis. Cell. Mol. Life Sci. *80*, 379. https://doi.org/10.1007/s00018-023-05032-y.

74. Kotsiliti, E., Leone, V., Schuehle, S., Govaere, O., Li, H., Wolf, M.J., Horvatic, H., Bierwirth, S., Hundertmark, J., Inverso, D., et al. (2023). Intestinal B cells license metabolic T-cell activation in NASH microbiota/antigen-independently and contribute to fibrosis by IgA-FcR signalling. J. Hepatol. *79*, 296–313. https://doi.org/10.1016/j.jhep.2023.04.037.

75. Greene, A.K., and Puder, M. (2003). Partial hepatectomy in the mouse: technique and perioperative management. J. Invest. Surg. *16*, 99–102. https://doi.org/10.1080/08941930390194424.

76. Marques, P.E., Antunes, M.M., David, B.A., Pereira, R.V., Teixeira, M.M., and Menezes, G.B. (2015). Imaging liver biology in vivo using conventional confocal microscopy. Nat. Protoc. *10*, 258–268. https://doi.org/10.1038/nprot.2015.006.

77. Andrews, S. (2010). FastQC: A Quality Control Tool for High Throughput Sequence Data.

78. Ewels, P., Magnusson, M., Lundin, S., and Käller, M. (2016). MultiQC: Summarize analysis results for multiple tools and samples in a single report. Bioinformatics *32*, 3047–3048. https://doi.org/10.1093/bioinformatics/btw354.

79. Krueger, F., James, F., Ewels, P., Afyounian, E., Weinstein, M., Schuster-Boeckler, B., Hulselmans, G., and sclamons. (2023). FelixKrueger/TrimGalore: v0.6.10 - add default decompression path (Zenodo). https://doi.org/10.5281/zenodo.7598955.

80. Dobin, A., Davis, C.A., Schlesinger, F., Drenkow, J., Zaleski, C., Jha, S., Batut, P., Chaisson, M., and Gingeras, T.R. (2013). STAR: ultrafast universal RNA-seq aligner. Bioinformatics *29*, 15–21. https://doi.org/10.1093/bioinformatics/bts635.

81. Li, B., and Dewey, C.N. (2011). RSEM: accurate transcript quantification from RNA-Seq data with or without a reference genome. BMC Bioinformatics *12*, 323. https://doi.org/10.1186/1471-2105-12-323.

82. Love, M.I., Huber, W., and Anders, S. (2014). Moderated estimation of fold change and dispersion for RNA-seq data with DESeq2. Genome Biol. *15*, 550. https://doi.org/10.1186/s13059-014-0550-8.

83. Kolberg, L., Raudvere, U., Kuzmin, I., Adler, P., Vilo, J., and Peterson, H. (2023). g:Profiler-interoperable web service for functional enrichment analysis and gene identifier mapping (2023 update). Nucleic Acids Res. *51*, W207–W212. https://doi.org/10.1093/nar/gkad347.

84. Zheng, G.X.Y., Terry, J.M., Belgrader, P., Ryvkin, P., Bent, Z.W., Wilson, R., Ziraldo, S.B., Wheeler, T.D., McDermott, G.P., Zhu, J., et al. (2017). Massively parallel digital transcriptional profiling of single cells. Nat. Commun. *8*, 14049. https://doi.org/10.1038/ncomms14049.

85. Weibel, E.R., Stäubli, W., Gnägi, H.R., and Hess, F.A. (1969). Correlated morphometric and biochemical studies on the liver cell. I. Morphometric model, stereologic methods, and normal morphometric data for rat liver. J. Cell Biol. *42*, 68–91. https://doi.org/10.1083/jcb.42.1.68.

86. Hao, Y., Hao, S., Andersen-Nissen, E., Mauck, W.M., 3rd, Zheng, S., Butler, A., Lee, M.J., Wilk, A.J., Darby, C., Zager, M., et al. (2021). Integrated analysis of multimodal single-cell data. Cell *184*, 3573–3587. e29. https://doi.org/10.1016/j.cell.2021.04.048.

87. Hafemeister, C., and Satija, R. (2019). Normalization and variance stabilization of single-cell RNA-seq data using regularized negative binomial regression. Genome Biol. *20*, 296. https://doi.org/10.1186/s13059-019-1874-1.

88. Aran, D., Looney, A.P., Liu, L., Wu, E., Fong, V., Hsu, A., Chak, S., Naikawadi, R.P., Wolters, P.J., Abate, A.R., et al. (2019). Reference-based analysis of lung single-cell sequencing reveals a transitional profibrotic macrophage. Nat. Immunol. *20*, 163–172. https://doi.org/10.1038/s41590-018-0276-y.

89. Heng, T.S.P., and Painter, M.W.; Immunological; Genome; Project Consortium (2008). The Immunological Genome Project: networks of gene expression in immune cells. Nat. Immunol. *9*, 1091–1094. https://doi.org/10.1038/ni1008-1091.

90. Guilliams, M., Bonnardel, J., Haest, B., Vanderborght, B., Wagner, C., Remmerie, A., Bujko, A., Martens, L., Thoné, T., Browaeys, R., et al. (2022). Spatial proteogenomics reveals distinct and evolutionarily conserved hepatic macrophage niches. Cell *185*, 379–396.e38. https://doi.org/10.1016/j.cell.2021.12.018.

91. Street, K., Risso, D., Fletcher, R.B., Das, D., Ngai, J., Yosef, N., Purdom, E., and Dudoit, S. (2018). Slingshot: cell lineage and pseudotime inference for single-cell transcriptomics. BMC Genomics *19*, 477. https://doi.org/10.1186/s12864-018-4772-0.

92. Amezquita, R.A., Lun, A.T.L., Becht, E., Carey, V.J., Carpp, L.N., Geistlinger, L., Marini, F., Rue-Albrecht, K., Risso, D., Soneson, C., et al. (2020). Orchestrating single-cell analysis with Bioconductor. Nat. Methods *17*, 137–145. https://doi.org/10.1038/s41592-019-0654-x.

93. Lange, M., Bergen, V., Klein, M., Setty, M., Reuter, B., Bakhti, M., Lickert, H., Ansari, M., Schniering, J., Schiller, H.B., et al. (2022). CellRank for directed single-cell fate mapping. Nat. Methods *19*, 159–170. https://doi.org/10.1038/s41592-021-01346-6.

94. Reuter, B., Fackeldey, K., and Weber, M. (2019). Generalized Markov modeling of nonreversible molecular kinetics. J. Chem. Phys. *150*, 174103. https://doi.org/10.1063/1.5064530.

95. Kharchenko, P.V., Silberstein, L., and Scadden, D.T. (2014). Bayesian approach to single-cell differential expression analysis. Nat. Methods *11*, 740–742. https://doi.org/10.1038/nmeth.2967.

96. Alquicira-Hernandez, J., and Powell, J.E. (2021). Nebulosa recovers single-cell gene expression signals by kernel density estimation. Bioinformatics *37*, 2485–2487. https://doi.org/10.1093/bioinformatics/btab003.

STAR★METHODS

KEY RESOURCES TABLE

REAGENT or RESOURCE	SOURCE	IDENTIFIER
Antibodies		
CD8-BV605	BioLegend	Cat#100744; clone:Clone53-6.7; host:Rat; RRID:AB_2562917
CD19–BUV395	BD Bioscience	Cat#563557; RRID: AB_2722495; host:human
CD4–BV510	BioLegend	Cat#100559; Clone:RM4-5; host:Rat; RRID: AB_2563781
CD45–PerCP-Cy5.5	BioLegend	Cat#103132; Clone:30-F11; host:Rat; RRID: AB_493558
CD4–BV711	BioLegend	Cat#100557; Clone:RM4-5; host:Mouse; RRID: AB_2562617
NK1.1–PerCP-Cy5.5	Mouse, BD Bioscience	Cat#551114; RRID: AB_394052
CD19–BUV395	BD Bioscience	Cat#563557; RRID:AB_2722495, host:Rat
CD62L–BUV737	BD Bioscience	Cat#612833; host:Rat; RRID: AB_2872237
CD45.2–Alexa Fluor 700	BioLegend	Cat#109822; Clone:104; host:Mouse; RRID: AB_2562614
NK1.1–BV605	BioLegend	Cat#108740; Clone:PK136; host:Mouse; RRID: AB_2562453
CD11b–APC	BioLegend	Cat# 101212; Clone:M1/70; host: Rat; RRID: AB_312795
CD44–Alexa Fluor 700	BioLegend	Cat#103026; Clone#IM7; host:Rat; RRID: AB_493739
CD4–BV510	BioLegend	Cat#100559; Clone:RM4-5; host:Rat; RRID: AB_2563781
CD45–PerCP-Cy5.5	BioLegend	Cat#103132; Clone:30-F11; host:Rat; RRID: AB_493558
CD8-PE	BioLegend	Cat#100708; Clone:53-6.7; host:Rat; RRID: AB_312750
Ly6G-APC-Cy7	BioLegend	Cat#127624; Clone:1A8; host:Rat; RRID: AB_2564290
Ly6C-BV605	BioLegend	Cat#128036; Clone:HK1.4; host:Rat; RRID: AB_2563796
IFNγ–APC	BioLegend	Cat#505810; Clone:XMG1.2; host:Rat; RRID: AB_315434
TNFα-FITC	BioLegend	Cat#506304; Clone:MP6-XT22; host:Rat; RRID: AB_315402
mouse of anti-CD8 antibody	BioXcell	Cat#BE0061; Clone 2.43,; host:Mouse; RRID: AB_1107636
anti-NK1.1 antibody	BioXcell	Cat#BE0036; Clone PK136; host:Mouse; RRID: AB_1107709
Biological samples		
Human Peripheral Blood Leukopak, Fresh	Stem Cell	Cat#200-0092
Chemicals, peptides, and recombinant proteins		
mouse recombinant IL-6 (E.Coli,)	R and D system	Cat#406-ML
clodronate liposomes	chemically synthesized, Liposoma BV	SKU: C-005
Deposited data		
Bulk RNA sequencing data	na	GEO: GSE283252
Single-cell RNA sequencing data	na	GEO: GSE283288
Custom code	na	https://doi.org/10.5281/zenodo.15001737
Experimental models: Cell lines		
RAW 264.7 cells	Sigma	Cat#91062702, (male BALB/c mouse)
Experimental models: Organisms/strains		
Mouse, strain: *Chat-GFP* reporter, B6.Cg-Tg(RP23-268L19-EGFP)2Mik/J	The Jackson Labratory	Strain #007902
Mouse, *Chat*^{flox}, B6.129-*Chat*^{tm1Jrs}/J	The Jackson Labratory	Strain #016920
Mouse, *Mb1-cre*, B6.C(Cg)-*Cd79a*$^{tm1(cre)Reth}$/EhobJ	The Jackson Labratory	Strain #020505
Mouse, *Cd4-cre*, Tg(Cd4-cre)1Cwi/BfluJ	The Jackson Labratory	Strain #017336
Mouse, Chrna7$^{-/-}$, B6.129S7-*Chrna7*^{tm1Bay}/J	The Jackson Labratory	Strain #003232
Mouse, wild-type, C57BL/6J	The Jackson Labratory	Strain #000664
Software and algorithms		
Adobe Ilusstrator	na	N/A

EXPERIMENTAL MODEL AND STUDY PARTICIPANT DETAILS

Mouse strains

Chat-GFP reporter (B6.Cg-Tg(RP23-268L19-EGFP)2Mik/J), *Chat*^{flox} (B6.129-*Chat*^{tm1Jrs}/J), *Mb1- cre* (B6.C(Cg)-*Cd79a*$^{tm1(cre)Reth}$/EhobJ), *Cd4-cre* (Tg(Cd4-cre)1Cwi/BfluJ), α7 nAChR knockout (KO) (Chrna7$^{-/-}$; B6.129S7-*Chrna7*^{tm1Bay}/J), and wild-type (WT; C57BL/6J) mice were all purchased from the Jackson Laboratory and maintained in the animal facility at the Princess Margaret Cancer Centre. ChAT$^{flox;Mb1\text{-}Cre}$ and ChAT$^{flox;CD4\text{-}Cre}$ mice were derived in-house using standard crossing methods. All mice were housed in autoclaved microisolator cages placed on ventilated racks. Reverse osmosis drinking water was supplied through an automatic watering system. The light cycle was lights-off at 1800 h and lights-on at 0600 h. The ambient temperature was held at 22-23°C with a humidity of 40–60%. Mice were routinely fed on the irradiated 7012 Teklad LM-485 Mouse/Rat Sterilizable Diet. All animal used in this study were 8-12 weeks old male mice. All animals in these experiments were approved by the University Health Network (UHN) Animal Care Committee.

METHOD DETAILS

Partial hepatectomy and splenectomy of mice

For partial hepatectomy (PHX), laparotomy was performed on male mice of at least 8-12 weeks of age using isoflurane inhalation narcosis as previously described[33,75] To achieve 70% PHX, the right upper lobe, left upper lobe and left lower lobe of the liver together with gallbladder were resected via one-step ligature using a 5-0 polyester suture tie (B. Braun Surgical, S.A.). Sham operations were performed in an identical manner without ligating and removing liver lobes. Thereafter, the abdominal cavity and outer layer of skin were closed using 5-0 polyglycolic acid (HR13, B. Braun) or 4-0 polypropylene monofilament (DS16, B. Braun), respectively.[75]

For experiments involving splenectomy, the splenic artery and vein were ligated with a single- knot 5-0 suture and the whole spleen was resected. Mice were then subjected to 70% PHX as above. The abdominal cavity was irrigated with 0.9% NaCl and both abdominal layers were closed using a running 5-0 suture (Ethicon).[75]

To reduce the mild pain inflicted by surgery, mice were treated post-operatively with Metacam (Meloxicam) at 5mg/kg. PHX and sham surgeries were performed and analyses conducted at various timepoints post-PHX as indicated in the Figures. Mice exhibiting severe symptoms were humanely sacrificed according to the regulations of the Animal Resource Centre at the Princess Margaret Hospital, UHN and were considered to have died.

Serum analyses

At 24 hrs post-PHX or sham surgery, mice were weighed and anesthetized using avertin [2.5% (v/v) in dH2O]. Blood was drawn from anesthetized mice, and serum was prepared by standard methods and used for assays of AST, ALT and IL-6, as follows. To determine serum levels of ALT and AST, a Beckman Coulter AU480 Clinical Chemistry Analyzer was used in conjunction with the Beckman Coulter ALT OSR6107 assay or Beckman Coulter AST OSR6109 assay, respectively. For quality control (QC), Biorad Liquid Assay Multiqual Level 1 694 and Level 3 696 assessments were used. Analyses were performed by The Centre for Phenogenomics, Pathology Core, UHN.

For ELISA quantification of serum IL-6, the Quantikine™ ELISA mouse IL-6 Immunoassay kit (Cat. No. M6000B-1, R&D Systems) was used following the manufacturer's instructions. In brief, 50 μL of Assay Diluent RD1-14 was added to each well of a 96-well plate, followed by 50 μL of standard, control, or experimental sample. After 2 hrs incubation at room temperature (RT), wells were washed in wash buffer (provided by the manufacturer), 100 μL Mouse IL-6 Conjugate was added to each well, and plates were incubated for 2 hrs at RT. After washing with wash buffer, 100 μL Substrate Solution was added to each well, followed by 30 min incubation at RT in the dark. The enzymatic reaction was stopped by adding 100 μL Stop Solution. Absorbance at 450 nm was read using a Spectramax iD3 plate reader (Molecular Devices).

Cyclin D1 determinations by IHC staining and quantitative real time-PCR

To assess Cyclin D1 protein levels, mouse tissues were embedded in paraffin and sectioned into 4μm slices. Sections were deparaffinized and rehydrated in a series of decreasing % ethanol solutions. Endogenous peroxidase activity was blocked with 3% hydrogen peroxide for 10 min at RT. Antigen retrieval was completed using an Na citrate (pH6) solution. Non-specific binding was reduced by a 10 min incubation with animal-free blocker (Vector SP-5030). Cyclin D1 primary antibody (rabbit host; 1:600 dilution; Abcam; Cat. No. ab134175) was applied and incubation continued at RT for 1 hour. Sections were then incubated for 35 min at RT with HRP-conjugated secondary antibody (Vector; Cat. No. MP-7401). Slides were visualized using a 3,3'- diaminobenzidine solution (VECTSK4100) and counterstained with CAT hematoxylin (BioCare). Stained slides were scanned at 20X magnification using a Hamamatsu Photonics NanoZoomer 2.0-HT.

To evaluate Cyclin D1 mRNA levels, the total RNA was isolated from whole mouse livers at 24 hrs after PHX or sham surgery. *Cyclind1* mRNA levels (relative to *Gapdh*) were measured using the Universal SYBR Green One-Step Kit (Bio-Rad, California, USA).

H&E staining

Mouse tissues were embedded in paraffin and sectioned into 4μm slices. Sections were deparaffinized and rehydrated in a series of decreasing % ethanol solutions. Sections were sequentially stained in solutions of hematoxylin, differentiation buffer, bluing buffer and eosin, with water washes between each step. Stained sections were dehydrated by progressing to 100% ethanol and transitioned into xylene before being cover-slipped and scanned at 20X magnification using a Hamamatsu Photonics NanoZoomer 2.0-HT.

Isolation of liver lymphocytes

Mice were euthanized with CO_2 and immediately subjected to whole body perfusion with ice-cold PBS containing 10 mM EDTA. Liver tissues were resected, digested, disrupted and passed through a 70 μm strainer. Non-parenchymal liver cells were enriched by 300xg centrifugation and used for flow cytometric cell sorting as described below.

Generation of RAW 264.7α7-KO cells

RAW 264.7 cells were seeded in 96-well plates in DMEM medium and cultured for few days to reach the required confluence for experiments. To prepare the Cas9:guide solution, Cas9 and *Chrna7* guide RNA (GGUCAAGAACUACAACCCGC and GGUGAGCGGCUGCGAGUCGU; from Synthego) were preincubated in electroporation buffer provided in the Cell Line Nucleofector Kit SF (Lonza Bioscience; Cat. No. V4XC-2024) at RT for 10 min to allow Cas9:guide complexes to form. RAW 264.7 cells ($1x10^6$) were pelleted and resuspended in 450μl electroporation buffer and mixed with Cas9:guide solution. Electroporation was performed using a Nucleofector 4d instrument (Lonza) according to the manufacturer's instructions. Cells were rapidly recovered by adding pre-warmed complete DMEM. Cells were transferred into T75 culture flasks and cultured for 7 days at 37°C, 5% CO2, with degree of cell confluence monitored daily. After 7 days, the absence of *Chrna7* expression in RAW264.7$^{\alpha7\text{-KO}}$ cells was confirmed using flow cytometry.

Mass spectrometry of liver tissue

Total protein was extracted from liver tissues and resuspended at a concentration of 100 μL per 10mg initial sample weight of 50% acetonitrile, 50% water containing 0.1% formic acid. Chromatographic separation of proteins was performed using a Thermo Scientific Ultimate 3000 UHPLC system equipped with a Waters Acquity BEH HILIC column (3.0 mm x 150 mm, 1.7 μm particle size) and a compatible guard column. The column temperature was maintained at 40°C, and the autosampler was kept at 5°C. For each run, 10 μL of prepared sample was injected. The mobile phases consisted of solvent A (0.1% formic acid in water) and solvent B (0.1% formic acid in acetonitrile). The flow rate was set to 0.4 mL/min, and the gradient program was as follows: 0- 2 min, 50% solvent B; 2-3 min, linear gradient to 0% solvent B; 3-11 min: 0% solvent B; 11-11.5 min, linear gradient to 50% solvent B; 11.5-15 min, 50% solvent B.

Mass spectrometric analysis was conducted using a Thermo Scientific Q Exactive mass spectrometer with a HESI II source. The following parameters were used: spray voltage, 3.5 kV; capillary temperature, 320°C; sheath gas flow rate, 40; auxiliary gas flow rate, 20; spare gas flow rate, 5; S-Lens RF level, 55. Full scan mass spectrometry was performed with the following settings: m/z range, 100-500; resolution, 140,000; AGC target, 3e6; maximum injection time (IT), 200 ms; polarity, positive.

Parallel Reaction Monitoring (PRM)

Parallel reaction monitoring was used to analyze targeted compounds with the following settings: resolution, 17,500; AGC target, 2e5; maximum IT, 100 ms; inclusion list (m/z), 158.1176 (acetylcholine), 150.1427 (acetylcholine-d4); isolation window, 0.4 m/z; normalized collision energy, 35. Targeted data analysis was performed using Thermo Scientific Xcalibur Qual Browser version 4.5. Fragment ion transitions used for identification were acetylcholine, 158.1176 → 87.0445; acetylcholine-d4, 150.1427 → 91.0697. Data were processed within a ±5 ppm error tolerance to ensure accuracy in identifying targeted compounds.

Flow cytometric cell sorting and cytokine detection

For staining of surface markers on non-parenchymal liver cells, the following fluorescently-tagged anti-mouse antibodies were used at a 1:100 dilution: CD8-BV605 (100744), CD19–BUV395 (563557), CD4–BV510 (100559), CD45–PerCP-Cy5.5 (103132), CD4–BV711 (100557), NK1.1– PerCP-Cy5.5 (551114), CD19–BUV395 (563557), CD62L–BUV737 (612833), all from BD Bioscience; CD45.2–Alexa Fluor 700 (109822), NK1.1–BV605 (108740), CD11b–APC (101212), CD44–Alexa Fluor 700 (103026), CD4–BV510 (100559), CD45–PerCP-Cy5.5 (103132), CD8- PE (100708), Ly6G-APC-Cy7 (127624), Ly6C-BV605 (128036), IFNγ–APC (505810) and TNFα-FITC (506304), all from Bio Legend.

For intracellular staining, non-parenchymal cells were stimulated *in vitro* for 4hrs with 25 μg/ml phorbol myristate acetate plus 1 mg/ml ionomycin (PMA/iono) in the presence of BD GolgiPlug. After staining for surface markers as above, cytokines were detected using the appropriate Cytofix/Cytoperm kits (BD) in accordance with the manufacturer's instructions. Flow cytometric analyses were performed using BD LSRFortessa instruments at the Princess Margaret Flow Facility, UHN.

Cytokine detection following in vitro ACh treatment

For liver cell experiments, $CD8^+$ T cells were sorted from among non-parenchymal liver cells as described above. Isolated $CD8^+$ T cells were seeded in 96-well plates at a density of $3x10^5$ cells/well. Cells were treated (or not) for 1hr at 37°C with varying concentrations of acetylcholine (ACh; Cat. No. A2661, Sigma) in the presence of the acetylcholinesterase inhibitor pyridostigmine

(150 mM final concentration; MedChemExpress, Cat. No. HY-B0207A).[49] These $CD8^+$ T cells were then stimulated (or not) for 3 hrs with PMA/iono (25 μg/ml;1 mg/ml, respectively) as above. Activated $CD8^+$ T cells were intracellularly stained to detect IFNγ production as described above. For experiments involving RAW264.7 cells, RAW 264.7^{wt} and RAW264.7$^{\alpha7\text{-ko}}$ cells were seeded in 96-well plates at a density of 1M cells. Cells were treated (or not) for 3 hrs with 0.5, 5, 10 or 15 mM ACh plus pyridostigmine (150 mM final concentration). As a positive control, cells were stimulated for 3 hrs with LPS (50ng/ml). Stimulated cells were stained intracellularly to detect IL-6 as above.

Phospho-specific flow cytometry

For liver cell experiments, liver lymphocytes were isolated as described above and $10x10^6$ were seeded in 96 wells plates and cultured in complete RPMI containing 10% heat-inactivated FBS, penicillin/streptomycin and L-glutamine. Plates were stained for 1 hr with anti-CD3-PE (clone 145-2c11) and anti-CD8-BV421 (clone 53-6.7) antibodies. Stained cells were then treated for 1 hr with 500 μM ACh plus 150 mM pyridostigmine as described above. Treated cells were stimulated with PMA/iono (25 μg/ml;1 mg/ml) for 5 min at 37°C. Stimulated cells were fixed with 2% paraformaldehyde (PFA) for 20 min on ice, washed with FACS buffer, and permeabilized using BD Phospho-flow Perm Buffer III (Cat. No. 558050). Permeabilized cells were washed and stained with antibodies targeting phospho-ERK1/2 (T202/Y204; clone D13.14.4E) or phospho-AKT (S473; clone D9E), followed by secondary detection using a goat-anti-rabbit F(ab) fragment conjugated with Alexa fluor 647 (Jackson Immunoresearch Cat. No. 111-607-008). Cells were washed, resuspended in FACS buffer, and examined on a Fortessa LSRII instrument. For experiments involving RAW 264.7 cells, RAW 264.7^{wt} and RAW 264.7$^{\alpha7\text{-ko}}$ cells were incubated with 0, 0.1, 0.25, 0.5, 1, 2.5, 5, 10, 25 or 50 mM ACh plus 150 mM pyridostigmine for 4 hrs at 37°C, 5% CO_2. Treated cells were washed and fixed as above. Fixed cells were washed, resuspended in 25 μL BD Phosphoperm buffer (ice cold), and permeabilized for 2 min on ice. Permeabilized cells were washed, resuspended in 25 μL p-STAT3 (Y705) #1297 prepared at 1:25 in FACS buffer (no azide), and incubated overnight at 4°C. Cells were then washed with 200 μL FACS buffer and pelleted by centrifugation at 2000xg for 5 min at 4°C, followed by gentle aspiration of the supernatant. Cells were resuspended in 50 μL secondary goat-anti-rabbit F(ab') fragment Alexa 647 1:2000 in FACS buffer and incubated at 4°C for 1 hour. Cells were washed with 200 μL FACS buffer, pelleted at 2000xg, 5 min, 4°C, and resuspended in FACS buffer. Samples were stored at 4°C until examination on BD LSRFortessa™ Flow Cytometer.

Adoptive transfer

To deplete Kupffer cells from mice *in vivo*, α7 knockout (KO) mice (8-12 weeks old) received intraperitoneal (i.p.) administration of 50 μL clodronate liposomes[39] (from Liposma BV). After 48 hrs, candidate rescue cells were prepared by isolating $Ly6^+$ monocytes from bone marrow, and $CD8^+$ T cells from spleens, of $CD45.1^+$ WT mice using either the EasySep™ Mouse Monocytes Isolation Kit (Cat. No. 19861) or the EasySep™ Mouse $CD8^+$ T Cell Isolation Kit (Cat. No.19858RF), respectively, following the manufacturer's protocol in both cases. For the rescue experiment, $10x10^6$ $CD8^+$ T cells, with or without $1x10^6$ $Ly6^+$ monocytes, were resuspended in a final volume of 200μl sterile PBS and injected i.v. into α7 KO recipient mice. After 48 hrs, these mice underwent 70% PHX and their survival was monitored for 12 days. For restore B cell ChAT expression to ChAT$^{flox;Mb1\text{-}Cre}$ mice, adoptive transfer of WT B cells was performed. Briefly, ($10x10^6$) splenic B cells were isolated from the spleen of WT $CD45.1^+$ mouse using a Stem Cell kit (Cat.No. 19854). Splenic B cells ($10x10^6$) were i.v.-injected into ChAT$^{flox;Mb1\text{-}Cre}$ mice 48 hrs prior to PHX, with another dose of $10x10^6$ splenic B cells administered by i.p. injection right before PHX.

In vivo depletion of $CD8^+$, NK1.1+ and Kupffer cells and IL-6 injection

To deplete $CD8^+$ or NK1.1 cells, mice received two intravenous (i.v.) doses of either 200 μg/mouse of anti-CD8 antibody (clone 2.43, BioXCell), or 600 μg of anti-NK1.1 antibody (clone PK136, BioXCell), on day 3 and day 1 prior to PHX or sham surgery.

To deplete Kupffer cells, mice were treated intraperitoneally (i.p.) with 200 μL of clodronate liposomes at 48hrs prior to PHX as described above.

For *in vivo* IL-6 injections, mice were treated i.p. with 5 μg/mL of mouse recombinant IL-6 (Cat. No. 78052.2, Stem Cell) both 24 hrs prior to PHX and immediately after the procedure. In all the above cases, mouse survival was monitored over 12 days.

Intravital microscopy of liver tissuesAdult C56BL/6 and ChAT^{BAC}-eGFP (B6.Cg-Tg(RP23-268L19-EGFP)2Mik/J) male mice were anesthetized by i.p. injection of ketamine (200 mg/kg body weight; Bayer Animal Health) and xylazine (10 mg/kg body weight; Bimeda-MTC). The following fluorescent-conjugated antibodies were injected i.v. (2mg/mouse) prior to surgery: rat anti-mouse F4/80 PE – clone BM8 (Invitrogen #12-4801-82, Lot 2514980), rat anti-mouse CD45R APC – clone RA3-6B2 (Invitrogen #17-0452- 82, Lot 4329236), and rat anti-mouse CD8a BV421 – clone 53-6.7 (BD Bioscience #563898, Lot 4267507). Surgery and preparation for liver intravital microscopy were performed as previously described.[76]

Images were acquired using an inverted spinning disk confocal microscope (Nikon Ti2-E; Yokogawa CSU-X1) equipped with a Prior SP450 Piezo Z focus drive and a motorized stage for live movement along the x- and y-axes. The microscope featured a motorized objective turret equipped with the following objective lenses: CFI60 PLAN APOCHROMAT Lambda D 10x/0.45 and CFI60 PLAN APOCHROMAT Lambda D 20x/0.8. Excitation parameters were based on the Toptica iChrome multi-laser engine (MLE-LFA-NI2) with wavelengths of 405 nm, 488 nm, 561 nm and 640 nm, combined with emission capture by Chroma ET455/50M, ET525/36M, ET605/52M, ET705/72M filters and the Chroma 89101M DAPI/FITC/TRITC/Cy5 quad-bandpass filter set. Imaging detection was performed using a Hamamatsu ORCA-Fusion BT CMOS camera. NIS element software (Nikon) was used to drive the confocal microscope and further acquisition and analysis of images. For analysis of cellular interactions, images of 5 areas of the liver per mouse

were taken for each of three WT mice at 4 hrs post-PHX. Total B cell, $CD8^+$ T cell and Kupffer cell numbers were counted, as were the frequencies of their interactions. Total interactions were then normalized to the total B cell count.

Norepinephrine and LPS in vitro stimulations of human PBMCs and mouse B cells

Peripheral blood mononuclear cells (PBMCs) ($1x10^6$) from healthy human volunteer donors, or splenic WT mouse B cells ($1x10^6$; isolated using the EasySep™ Mouse B Cell Isolation Kit, Cat.No. 19854RF). Human PBMCs were seeded in wells of 96-well V bottom plates in 100 μL IMDM containing 10% H.I. FBS, glutamax (5 mL), pen/strep (5 mL), gentamicin (10 μg/mL, final), non-essential amino acids (NEAA) (5 mL), 500 μL 2-me. Mouse splenic B cells were seeded in wells of 96-well V bottom plates in 100 μL DMEM containing 10% H.I. FBS, pen/strep (5 mL).

Each well received either 100 μL norepinephrine (NE; 10 or 100 ng/ml), LPS (5 or 20 ng/ml), or anti-IgM antibody (1 or 10 μg/ml). Plates were incubated for 4 hrs at 37°C, 5% CO_2 prior to staining for 1hr with antibodies recognizing the cell surface markers CD19 or B220, as well as with the viability dye eFluor™ 780 (APC-Cy7). Stained cells were washed, pelleted by centrifugation for 5 min at 1200 rpm at 4°C, and fixed by resuspension in 50 μL 4% PFA in PBS, followed by incubation for 10 min at 4°C. Cells were washed with 1X BD Permwash (Cytofix/Cytoperm kits; BD) in accordance with the manufacturer's instructions and pelleted at 1200 rpm, 5 min, 4°C. Cells were resuspended in 25 μL anti-ChAT Chicken IgY (#1319, Thermo Fisher Scientific; stored at 4°C) prepared 1:25 in 1x BD Permwash and incubated at 4°C overnight. The following day, cells were washed with BD Permwash and pelleted at 1200 rpm, 5 min, 4°C. Cells were resuspended in 25 μL anti-Chicken FITC (#166, Thermo Fisher Scientific; 1:200 in 1X Permwash) and incubated at 4°C overnight. Cells were washed the next day, pelleted at 1200 rpm, 5 min, 4°C, and resuspended in 200 μL FACS buffer. Samples were stored at 4°C until examination on BD LSRFortessa™ Flow Cytometer.

mRNA expression of nicotinic and muscarinic ACh receptor genes

Non-parenchymal cells were isolated from mouse livers as above. $CD8^+$ T cells and Kupffer cells were sorted either on a BD FACSAria Fusion flow cytometric cell sorter at the Princess Margaret Flow Facility, or in-house using the Easy Sep CD8a Selection kit ($CD8^+$ T cells; StemCell Cat. No. 18953) or the F4/80 Mouse Positive Selection kit; StemCell Cat. No. 00-0659). RNA was extracted from sorted cells using an RNAeasy microkit (QIAGEN Cat. No. 74034) according to the manufacturer's instructions. Quantitative PCR was used to measure the levels of muscarinic (m) and nicotinic (n) AChR cDNAs by standard methods.

Flow cytometric determination of surface expression of nAChR and mAChR proteins

After sorting as above, $CD8^+$ T cells were seeded in 96-well plates (~$2x10^6$/well) and centrifuged at 1500 rpm for 5 min at 4°C. FC block (BD Pharmagen Cat. No. 553142) was prepared in FACS buffer (1:100 diluted in PBS + 2% FBS). Cells were then resuspended in FC block solution and incubated for 30 min at 4°C. Blocked cells were washed in FACS buffer, resuspended in 25 μL anti-α7 nAChR antibody (#ANC-007) in PBS + 2% FBS, and incubated for 1hr at 4°C. After washing in FACS buffer, cells were subjected to secondary antibody staining by resuspending them in 50 μL goat anti-rabbit F(ab') fragment A647 (1:2000 in PBS + 2% FBS) followed by incubation for 30 min at 4°C. Cells were washed, resuspended in 50 μL 4% PFA (ThermoFisher Scientific J61899.AP), and incubated for 10 min at 4°C. Cells were washed and resuspended in FACS buffer for analysis by flow cytometry as described above.

B cell isolation, mRNA library construction, and bulk RNA sequencing

ChAT-GFP reporter mice were subjected to 70% PHX or sham surgery, and liver non-parenchymal cells were enriched as described above. B cells were stained and sorted on a BD FACSAria Fusion flow cytometry cell sorter at the Princess Margaret Flow Facility. RNA was extracted using the RNAeasy micro kit (QIAGEN) based on the manufacturer's instructions. Extracted RNAs were submitted to the Princess Margaret Genomics Centre for downstream processing. Sample library preparation was performed using a Mammalian Low Input V2 Pico kit (Takara). Sequencing was performed on an Illumina Novaseq 6000 using a 200-cycle, paired end protocol to obtain ~40 million reads/sample.

Immune repertoire reconstruction from bulk RNA sequencing

The TRUST4[23] algorithm (accessed September 5, 2024) was used to reconstruct the immune repertoire from the. fastq files derived from bulk RNA sequencing of B cells. Trimmed reads were aligned to the provided mm10 BCR/TCR gene and IMGT references, and repertoires assembled using default parameters. Sample purity was confirmed by the presence of negligible TCR reconstruction. Gene usage for a particular CDR3 sequence was imputed in instances where the gene usage was not determined by TRUST4 in only one of the two samples from the same mouse.

Alignment, processing, and analysis of ChAT+ B cell bulk RNA sequencing data

The quality of individual raw fastq files was determined using FastQC (v 0.11.8)[77] and aggregated using MultiQC (v 1.6)[78]. Adaptor content was trimmed using Trim Galore (v 0.6.6) on paired reads with default parameters.[79] Trimmed reads were then aligned to the mm10_STAR_2.7.9a mouse reference using STAR (v 2.7.9a),[80] with –quantMode GeneCounts TranscriptomeSAM. Gene counts and transcripts per million (TPM) normalization were determined using RSEM (v 1.3.0)[81]. Differential expression testing, variance stabilizing transformation (VST), and PCA analysis were performed on aggregated

STAR aligned count files using DESeq2 (v 1.38.3)[82]. Full lists of genes that were significantly (FDR < 0.05) differentially expressed between ChAT^{+} and ChAT^{-} B cells from sham- or PHX-treated mice can be found in Tables S1, S2, and S3 (see Tables S1, S2, and S3).

Pathway enrichment analysis

Genes that were differentially expressed between ChAT-GFP^{+} B cells at 4 hrs post-PHX and other conditions were determined using DESeq2 as described above. Significantly (FDR < 0.05) differentially expressed genes with a $\log_2$-fold change greater than 0.5 and less than -0.5 were separately queried using g:Profiler.[83] Only pathways from KEGG, Reactome (REAC), and WikiPathways (WP) that achieved a B-H FDR < 0.1 were considered. A full list of enriched pathways is provided in Table S4 (See Table S4).

Single-cell RNA sequencing (scRNAseq) library preparation, sequencing, and alignment

ChAT^{flox} and ChAT$^{flox;Mb1\text{-}Cre}$ mouse livers were collected at 2, 4, and 24 hours after PHX or sham surgery, and 25mg of tissue from the same lobe across experimental samples were immediately snap-frozen. Samples were then submitted to the Princess Margaret Genomics Centre for downstream processing. Thawing and dissociation of cell samples were performed according to the Tissue Fixation & Dissociation for Chromium Fixed RNA Profiling protocols provided by 10X Genomics. Sample probe hybridization, washing, pooling, and capture of approximately10,000 cells per sample, 4 samples per library (2 libraries), and followed by library construction, were performed according to 10X Genomics protocols for the 4-plex kit. The sequencing was performed using an Illumina NovaSeq 6000 targeting 2400B reads total (approximately 30,000 reads/cell). Raw fastq files were aligned to the mm10-2020-A mouse reference using CellRanger (v7.0.0)[84] multi, with the probe-set Chromium_Mouse_Transcriptome_Probe_Set_v1.0_mm10-2020-A.csv.

Quality control and normalization of scRNAseq libraries

Quality control (QC) of scRNAseq data typically consists of identifying and excluding cells with a high proportion of mitochondrial gene transcripts (indicative of damaged or dying cells) and/or cells with a high library size (i.e. high transcript count indicative of artificial doublets). However, hepatocytes can have a naturally high mitochondrial content, and naturally occurring polyploid hepatocytes are expected to have a high library size.[29,85] With these considerations in mind, we utilized a two-step QC procedure that was performed using Seurat (v 4.3.0)[86] in the R (v 4.2.2) statistical environment. Cells with fewer than 200 expressed genes were excluded, and a lenient threshold of three median absolute deviations (MAD) was used to exclude poor-quality cells based on mitochondrial content. The remaining cells were normalized using SCTransform (v 0.3.5)[87] with the following arguments: method = "glmGamPoi", vst.flavor = "v2", variable.features.n = 3000, return.only.var.genes = F, and regressing unwanted variation associated with mitochondrial content (vars.to.regress = "percent.mt"). UMAP embeddings were calculated, and cell clusters were identified using Seurat's shared-nearest neighbor algorithm following modularity optimization using the Louvain algorithm with multilevel refinement. Only the first 20 principal components (PCs) were used along with a low clustering resolution of 0.2 to identify only dominant (macro) cell types. Secondly, on a per cluster basis, cells with RNA content one MAD over the median were excluded. This restriction allowed for the exclusion of likely doublets on a per-cell type basis, while retaining diploid and polyploid hepatocytes with a natural bimodal distribution of RNA content.

Integration and cell type annotation of scRNAseq libraries

The remaining high-quality cells from each sample above were merged and integrated using Seurat's canonical correlation analysis (CCA) anchoring method. Clustering and dimensionality reduction using UMAP were performed with the first 14 PCs as described above but now using a higher clustering resolution of 2 to identify more minute cell types and states. Clusters of cells were annotated based on the expression of canonical gene markers, following differential expression analysis using Seurat's FindAllMarkers with default parameters (Figure S6B). A full list of differentially expressed genes can be found in Table S5.

Hepatic immune cell sub-clustering

To examine the full spectrum of immune cells present in the liver, immune cell types (Kupffer cells, Neutrophils, Monocytes and DCs, B cells, and T cells) were sorted into subsets and re- clustered using the methods described above and a clustering resolution of 1. Clusters of cells were re-annotated using a combination of methods. SingleR (v 2.0.0)[88] was used to provide an unbiased annotation based on transcriptional similarity to the ImmGen[89] reference. However, the ImmGen reference does not contain a transcriptional profile for Kupffer cells. To supplement the ImmGen-based annotations, we leveraged the Liver Cell Atlas[90] to identify clusters corresponding to Kupffer cells, Monocytes, cDCs, and pDCs. A full list of significantly differentially expressed genes for hepatic immune cells can be found in Table S6.

Kupffer cell pseudotime trajectory analysis

To examine the dynamic relationship between Kupffer cell transcriptional phenotype and response to PHX in cells from ChAT^{flox} and ChAT$^{flox;Mb1\text{-}Cre}$ mice, we used the pseudotime inference method called SlingShot (v 2.6.0)[91]. Briefly, Kupffer cells were subset from the hepatic immune cell sub-cluster dataset and converted from Seurat into a SingleCellExperiment object (v 1.20.1)[92]. Only highly expressed genes were retained by applying a threshold of at least 1.5 normalized counts in at least 5 cells, resulting in 1,772 genes. SlingShot was performed with default clusters on the UMAP embedding, and the resulting pseudotime trajectories were merged. Per

cell pseudotime values from SlingShot were used as the basis for constructing and plotting a PseudotimeKernel using CellRank (v 2.0.2)[93] implemented in Python (v 3.9.6) (Figure 3A). A Generalized Perron Cluster Cluster Analysis (GPCCA)[94] estimator was computed to determine initial and terminal Kupffer cell states, which were used to determine significant lineage driver genes. A full list of lineage driver genes can be found in Table S5.

Single-cell gene expression density visualizations

In scRNAseq, genes with apparent low expression and/or low detection rates are more significantly affected by gene drop-out events,[95] resulting in false negative expression. In these cases, it can be useful to examine gene expression density—in other words, cell neighborhoods containing multiple positive cells—to account for potential dropout.[96] We used Nebulosa (v 1.8.0) to calculate and plot gene-weighted kernel density estimations to leverage neighbor cell information and alleviate the effects of drop-out.[96]

Analysis of scRNAseq and spatial transcriptomics of liver regeneration

For data acquisition, the processed scRNAseq liver regeneration atlas and Stereo-seq samples from Xu et al.[40] were downloaded from the STOmicsDB LISTA portal (https://db.cngb.org/stomics/lista/download/). Cell type annotations for the scRNAseq liver regeneration atlas and zonal annotations from the Stereo-seq samples were used consistently throughout our analysis.

For spatial spot deconvolution, we considered the fact that each spatially resolved spot in the Stereo-seq samples accessed from Xu et al. represents a handful of cells present within each 36 x 36 μm bin, rather than a single cell.[40] Thus, to infer the cell types present in each spatial spot, we performed cell type deconvolution following a method similar to that performed in Xu et al. Briefly, the spatial coordinates and gene expression data from each homeostatic and post-PHX section (from 8 to 72 hours post-PHX) were iteratively extracted to construct query objects using the *SpatialRNA* function from spacexr (v 2.2.1).[48] Matched timepoint cell type references were created using the *Reference* function after segregating the scRNAseq liver regeneration atlas data by timepoint post-PHX. Using a method unique to our analysis, such spatial sections were then deconvoluted using only cells derived from the same timepoint (e.g. spatial sections from 8 hours post-PHX were deconvoluted using only single cells derived from 8 hours post-PHX livers, etc.). Deconvolution was performed using the *create.RCTD* and *run.RCTD* functions with *doublet_mode = 'multi'.*

To evaluate cell type enrichment by gene expression pattern, deconvolution scores were extracted for each cell type for each Stereo-seq spatial section. Spatial spot barcodes with positive expression of each gene of interest were extracted and grouped by timepoint post-PHX. For each cell type and timepoint, the deconvolution scores of gene-positive and gene-negative barcodes were compared using a two-sided Wilcoxon Rank Sum test to detect significant enrichment of a certain cell type with a certain gene. As a control for this method, we assessed the statistical enrichment of Kupffer cells in spatial spots that expressed *Vsig4*, a Kupffer cell-specific marker both in our scRNAseq dataset (Figure S6A) and in the scRNAseq liver regeneration atlas (Figure S6B) of Xu et al.; we found significant enrichment at each timepoint (Figure S6A). Concomitantly with *p*- value calculations, a fold change was calculated as the mean deconvolution score of gene-positive barcodes divided by the mean deconvolution score of the gene-negative barcodes.

QUALIFICATION AND STATISTICAL ANALYSIS

For all flow cytometry results, GraphPadPrism 5.0 and FlowJo statistical analysis software tools were used. For all histology results, GraphPadPrism 5.0 and Fiji software were used. Unless otherwise indicated, data are presented as the mean ± SEM. For all bioinformatic analyses of bulk, single-cell, and spatial transcriptomics datasets, R (v 4.2.2) was used unless otherwise indicated.